10-9-2019

A volume-filtered description of compressible particle-laden flows

Gregory S. Shallcross
University of Michigan

Rodney O. Fox
Iowa State University, rofox@iastate.edu

Jesse Capecelatro
University of Michigan

A volume-filtered description of compressible particle-laden flows

Abstract
In this work, we present a rigorous derivation of the volume-filtered viscous compressible Navier–Stokes equations for disperse two-phase flows. Compared to incompressible flows, many new unclosed terms appear. These terms are quantified via *a posteriori* filtering of two-dimensional direct simulations of shock-particle interactions. We demonstrate that the pseudo-turbulent kinetic energy (PTKE) systematically acts to reduce the local gas-phase pressure and consequently increase the local Mach number. Its magnitude varies with volume fraction and filter size, which can be characterized using a Knudsen number based on the filter size and inter-particle spacing. A transport equation for PTKE is derived and closure models are proposed to accurately capture its evolution. The resulting set of volume-filtered equations are implemented within a high-order Eulerian–Lagrangian framework. An interphase coupling strategy consistent with the volume filtered formulation is employed to ensure grid convergence. Finally PTKE obtained from the volume-filtered Eulerian–Lagrangian simulations are compared to a series of two- and three-dimensional direct simulations of shocks passing through stationary particles.

Keywords
Eulerian–Lagrangian, Multiphase flow, Shock-particle interaction, Pseudo-turbulence

Disciplines
Chemical Engineering | Complex Fluids

Comments
This is a manuscript of an article published as Shallcross, Gregory S., Rodney O. Fox, and Jesse Capecelatro. "A volume-filtered description of compressible particle-laden flows." *International Journal of Multiphase Flow* (2019): 103138. DOI: 10.1016/j.ijmultiphaseflow.2019.103138. Posted with permission.

Journal Pre-proof

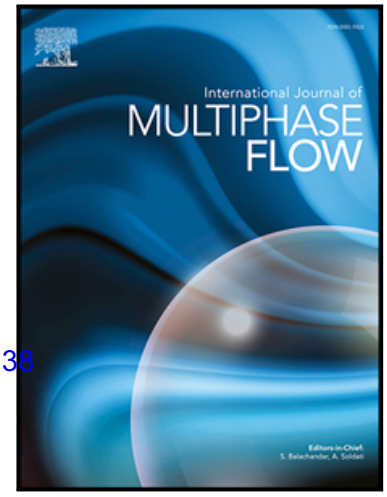

A volume-filtered description of compressible particle-laden flows

Gregory S. Shallcross, Rodney O. Fox, Jesse Capecelatro

PII: S0301-9322(19)30511-7
DOI: https://doi.org/10.1016/j.ijmultiphaseflow.2019.103138
Reference: IJMF 103138

To appear in: *International Journal of Multiphase Flow*

Received date: 16 July 2019
Revised date: 7 September 2019
Accepted date: 8 October 2019

Please cite this article as: Gregory S. Shallcross, Rodney O. Fox, Jesse Capecelatro, A volume-filtered description of compressible particle-laden flows, *International Journal of Multiphase Flow* (2019), doi: https://doi.org/10.1016/j.ijmultiphaseflow.2019.103138

Highlights

- Rigorous derivation of the volume-filtered compressible equations for two- phase flows
- Evaluate unclosed terms via a posteriori filtering of particle-resolved sim- ulations
- Propose a transport equation for PTKE and closure model for the dissipa- tion rate
- Grid convergence of the Euler-Lagrange framework is demonstrated on compressible flow
- The model captures pseudo-turbulent Reynolds stresses independently of the drag law

A volume-filtered description of compressible particle-laden flows

Gregory S. Shallcross[a,*], Rodney O. Fox[b], Jesse Capecelatro[a]

[a]*Department of Mechanical Engineering, University of Michigan, Ann Arbor, MI 48109-2125, USA*
[b]*Department of Chemical and Biological Engineering, Iowa State University, Ames, IA 50011-1098, USA*

Abstract

In this work, we present a rigorous derivation of the volume-filtered viscous compressible Navier–Stokes equations for disperse two-phase flows. Compared to incompressible flows, many new unclosed terms appear. These terms are quantified via *a posteriori* filtering of two-dimensional direct simulations of shock-particle interactions. We demonstrate that the pseudo-turbulent kinetic energy (PTKE) systematically acts to reduce the local gas-phase pressure and consequently increase the local Mach number. Its magnitude varies with volume fraction and filter size, which can be characterized using a Knudsen number based on the filter size and inter-particle spacing. A transport equation for PTKE is derived and closure models are proposed to accurately capture its evolution. The resulting set of volume-filtered equations are implemented within a high-order Eulerian–Lagrangian framework. An interphase coupling strategy consistent with the volume filtered formulation is employed to ensure grid convergence. Finally PTKE obtained from the volume-filtered Eulerian–Lagrangian simulations are compared to a series of two- and three-dimensional direct simulations of shocks passing through stationary particles.

Keywords: Eulerian–Lagrangian, Multiphase flow, Shock-particle interaction, Pseudo-turbulence

1. Introduction

Over the past several decades, significant progress has been made towards improving the numerical prediction of disperse multiphase flows (e.g., [2, 15, 58], and references therein). Yet, the majority of these efforts have focused on low-speed (incompressible) regimes. Two-phase flows that exhibit strong compressibility play dominant roles in nature, such as during supernovas and volcanic eruptions, in industry (coal dust explosions, shock wave lithotripsy, combustion/detonation, etc.) and space exploration (e.g., fluidization of terrestrial regolith during rocket plume-surface interactions [4, 17, 34]). Compared to their low-speed counterparts, particle-laden compressible flows like the examples listed here typically introduce new length- and time-scales and additional physics that further complicate modeling efforts.

As an illustrative example, consider the particle-laden shock-tube depicted in Fig. 1. A shock propagates through the fluid towards a collection of disperse particles (Fig. 1(a)). Shortly after it passes through (Fig. 1(b)), transmitted and reflected shocks form, wakes are generated (shown in grey), and the gas accelerates to supersonic speeds at the downstream edge of the particles. In recent years, significant attention has been made on

*Corresponding author
Email address: grshall@umich.edu (Gregory S. Shallcross)

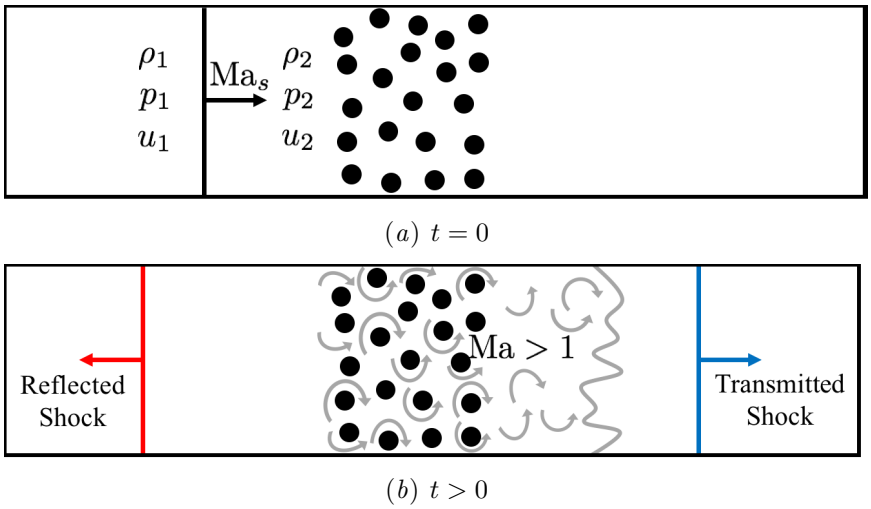

Figure 1: Schematic of a shock-particle interaction at an initial state (a) and some later time (b).

modeling two-way coupling of finite size particles [3, 8, 23, 26], yet accurate models capable of predicting the scenario illustrated in Fig. 1 remain elusive. Some of the challenges are attributed to the large slip velocities between the phases (which can be on the order of the sound speed), unsteadiness of the shockwave dynamics and associated wakes, and back-coupling from the solid phase to the gas.

Obtaining a mathematical description that captures the multi-scale nature of two-phase flows typically involves ensemble averaging [69] or volume filtering [1, 4, 8, 11]. Similar to single-phase flows, such efforts inevitably result in unclosed terms that require models. While some correlations obtained from experiments or particle-resolved direct numerical simulations (DNS) have a clear physical interpretation (e.g., the drag coefficient or heat transfer rate), their connection to model closure is not always obvious. This is especially true for high-speed flows whereby filtering or averaging the governing equations reveals unclosed terms that contain additional physics [35].

In the context of shock-particle interactions for moderately dilute and dense suspensions, small-scale velocity fluctuations are produced in particle interstitial sites and advected downstream with the mean flow [24, 35, 48] (see Fig. 1(b)). This results in subgrid-scale (or sub-filtered) velocity fluctuations that contribute to an unclosed term akin to the Reynolds stress that appears in single-phase flow, but here represents unresolved fluctuations due to the presence of particles. Because such fluctuations exist even in laminar flow (e.g., steady wakes), it is often referred to as *pseudo*-turbulent kinetic energy (PTKE). While this term is typically neglected in incompressible flows without significant consequence, recent DNS have shown that PTKE can contribute between 30% and 100% of the resolved kinetic energy in compressible flows [24, 35, 39, 48]. Its strength has been shown to increase as the particle volume fraction and the incident shock Mach number increase [35]. An algebraic model for the PTKE was recently proposed for incompressible homogeneous gas-solid flows [33] and compressible flows [39]. However, such models have only been tested under limited conditions and fail to predict PTKE in regions void of particles. Other models have been proposed based on cloud-in-cell approaches, where the unclosed subgrid-scale stresses are accounted for in the particle momentum balance using the so-called Subgrid Particle-Averaged Reynolds Stress-Equivalent (SPARSE) method [13, 56]. With the increase in available compressible

DNS data in recent years [35, 60, 61], new models valid in higher-speed regimes can be developed and tested. The aim of this study is to present a framework for developing and integrating such models.

In the following section, the volume-filtered compressible Navier–Stokes equations are derived, with specific attention paid to the unclosed terms appearing in the gas-phase energy equation and equation of state. DNS of shock-particle interactions under varying volume fractions are then presented, followed by an *a posteriori* analysis of the sub-filtered terms appearing in the volume-filtered equations. The equations are then implemented in a high-order Eulerian–Lagrangian framework. Grid convergence of the volume-filtered Eulerian–Lagrangian equations is demonstrated on a one-dimensional converging-diverging nozzle. A model is then proposed for the PTKE and validated against two- and three-dimensional particle-resolved simulations.

2. Volume filtered formulation

In this section, a rigorous derivation of the volume filtered equations is presented for viscous compressible two-phase flows. In particular, we extend the equations of motion presented by Anderson and Jackson [1] to the compressible regime. We begin by defining the microscale equations that represent a model-free description of a compressible fluid-particle system. A volume filter is then applied to these equations with a focus on discrepancies between low-Mach number formulations. In Sec. 3, direct simulations of the microscale equations are conducted to evaluate the sub-filtered (unclosed) terms that arise here.

2.1. Fluid-phase description at the microscale

The governing equations describing a viscous compressible flow are given by

$$\frac{\partial \rho}{\partial t} + \nabla \cdot (\rho \boldsymbol{u}) = 0, \tag{1}$$

$$\frac{\partial \rho \boldsymbol{u}}{\partial t} + \nabla \cdot (\rho \boldsymbol{u} \otimes \boldsymbol{u} + p\mathbb{I} - \boldsymbol{\tau}) = 0, \tag{2}$$

and

$$\frac{\partial \rho E}{\partial t} + \nabla \cdot (\{\rho E + p\}\boldsymbol{u} + \boldsymbol{q} - \boldsymbol{u} \cdot \boldsymbol{\tau}) = 0, \tag{3}$$

where each variable denotes a microscale quantity (i.e., a scalar or vector field at a scale smaller than an individual particle). Here, $\mathbb{I}$ is the identity matrix, ρ is the density, $\boldsymbol{u}$ is the velocity, p is the pressure, and E is the total energy. In this work, all variables are non-dimensionalized with the ambient density $\rho^\star_\infty$, a characteristic length scale $L^\star$, dynamic viscosity μ_∞, heat capacity at constant pressure $C^\star_p$, and speed of sound $c^\star_\infty = \sqrt{\gamma p^\star_\infty / \rho^\star_\infty}$ with $\gamma = 1.4$ the specific heat ratio and $p^\star_\infty$ the ambient pressure. All dimensional quantities are denoted by a superscript $\star$, and the subscript ∞ indicates a reference quantity (taken to be air at ambient conditions).

The non-dimensional viscous stress tensor can be expressed as

$$\boldsymbol{\tau} = \frac{\mu}{\mathrm{Re}_c}\left(\nabla \boldsymbol{u} + \nabla \boldsymbol{u}^\mathsf{T}\right) + \frac{\lambda}{\mathrm{Re}_c}\nabla \cdot \boldsymbol{u}, \tag{4}$$

and the non-dimensional heat flux is

$$\boldsymbol{q} = -\frac{\mu}{\mathrm{Re}_c \mathrm{Pr}}\nabla T, \tag{5}$$

where $\mathrm{Pr} \equiv C_p^\star \mu^\star / k^\star$ is the Prandtl number with $\mu^\star$ and $k^\star$ the dynamic viscosity and thermal conductivity, respectively. The Reynolds number based on the reference sound speed is defined as $\mathrm{Re}_c = \mathrm{Re}/\mathrm{Ma}_c$, where $\mathrm{Re} = \rho_\infty^\star U^\star L^\star / \mu_\infty^\star$ is the flow Reynolds number with $U^\star$ a characteristic velocity, and $\mathrm{Ma}_c = U^\star / c_\infty^\star$ is the reference Mach number. In this work, the non-dimensional viscosity is modeled as a power law $\mu = [(\gamma - 1)T]^n$, with $n = 0.666$ as a model for air. The second coefficient of viscosity is given by $\lambda = \mu_B - \frac{2}{3}\mu$ where the bulk viscosity $\mu_B = 0.6\mu$ is chosen as a model for bulk viscosity of air. The thermodynamic pressure, p, and temperature, T, are obtained via the equation of state for an ideal gas, given in non-dimensional form as

$$T = \frac{\gamma p}{(\gamma - 1)\rho} \quad \text{and} \quad p = (\gamma - 1)\left(\rho E - \frac{1}{2}\rho \boldsymbol{u} \cdot \boldsymbol{u}\right). \tag{6}$$

In the microscale description, interactions with the solid phase are incorporated by imposing no-slip and no-penetration boundary conditions at the surface of each particle, in addition to enforcing appropriate heat flux conditions.

2.2. Volume-filter operators

In order to account for the effect of particles without requiring to resolve the fluid-phase equations on the scale of the particle surface, the Navier–Stokes equations are split into microscale (sub particle-scale) processes, and mesoscale processes, i.e., processes that take place on a scale larger than the particle diameter. Following Anderson and Jackson [1], we begin by defining a filtering kernel $\mathcal{G}$ with a characteristic length δ_f, such that $\mathcal{G}(r) > 0$ decreases monotonically with increasing r, and is normalized such that its integral over the entire physical space is unity. The local voidage at a point $\boldsymbol{x}$ and time t is defined as

$$\alpha(\boldsymbol{x}, t) = \int_{\mathcal{V}} \mathcal{I}(\boldsymbol{y}) \mathcal{G}(|\boldsymbol{x} - \boldsymbol{y}|) \ \mathrm{d}\boldsymbol{y} = \int_{\mathcal{V}_f} \mathcal{G}(|\boldsymbol{x} - \boldsymbol{y}|) \ \mathrm{d}\boldsymbol{y}, \tag{7}$$

where $\mathcal{V}$ indicates that the integral is taken over all points $\boldsymbol{y}$ occupied by the fluid-particle system and $\mathcal{I}$ is an indicator function defined as

$$\mathcal{I}(\boldsymbol{y}) = \begin{cases} 1 & \text{if fluid} \\ 0 & \text{otherwise.} \end{cases} \tag{8}$$

To abbreviate the notation throughout the remainder of this section, the integral will be taken over $\mathcal{V}_f$, all points $\boldsymbol{y}$ occupied by the fluid. Taking $\delta_f \gg d_p$, with d_p the particle diameter, and assuming $\mathcal{G}$ varies little over the surface of a particle, the particle volume fraction can be expressed as

$$\alpha_p(\boldsymbol{x}, t) = 1 - \alpha \approx \sum_{i=1}^{N_p} \mathcal{G}\left(|\boldsymbol{x} - \boldsymbol{x}_p^{(i)}|\right) \mathcal{V}_p, \tag{9}$$

where N_p is the total number of particles in the system, and $\boldsymbol{x}_p^{(i)}$ and $\mathcal{V}_p$ is the position and volume of the i-th particle, respectively.

Any flow quantity $\boldsymbol{a}(\boldsymbol{x}, t)$ can be decomposed into filtered and sub-filtered components such that $\boldsymbol{a}(\boldsymbol{x}, t) = \overline{\boldsymbol{a}}(\boldsymbol{x}, t) + \boldsymbol{a}'(\boldsymbol{x}, t)$, where the volume filtered quantity is given by

$$\alpha \overline{\boldsymbol{a}}(\boldsymbol{x}, t) = \int_{\mathcal{V}_f} \boldsymbol{a}(\boldsymbol{y}, t) \ \mathcal{G}(|\boldsymbol{x} - \boldsymbol{y}|) \ \mathrm{d}\boldsymbol{y}. \tag{10}$$

For convenience in the following formulation, we introduce a Favre filtered quantity $\widetilde{\boldsymbol{a}} = \overline{\rho \boldsymbol{a}}/\overline{\rho}$. With this, any fluid property $\boldsymbol{a}$ can be split into its associated Favre averaged and residual components as $\boldsymbol{a} = \widetilde{\boldsymbol{a}} + \boldsymbol{a}''$. Unlike ensemble averaging, the filtering operation invokes local spacial averaging and consequently volume filtered quantities are stochastic in nature such that $\overline{\boldsymbol{a}'} \neq 0$ and $\widetilde{\boldsymbol{a}''} \neq 0$.

2.3. Volume-filtered equations

2.3.1. Filtered mass conservation

Volume filtering the microscale density equation (1) yields

$$\frac{\partial \alpha \overline{\rho}}{\partial t} + \nabla \cdot (\alpha \overline{\rho} \widetilde{\boldsymbol{u}}) = 0, \tag{11}$$

and requires no closure.

2.3.2. Filtered momentum

While the derivation of the volume-filtered momentum equation can be found elsewhere [1, 8, 11], special care needs to be taken when considering high-speed flows. For example, volume filtering the pressure gradient term in (2) yields

$$\int_{\mathcal{V}_f} \nabla p \mathcal{G}(|\boldsymbol{x} - \boldsymbol{y}|) \ \mathrm{d}\boldsymbol{y} = \nabla (\alpha \overline{p}) - \sum_{i=1}^{N_p} \int_{\mathcal{S}_i} \boldsymbol{n} p \mathcal{G}(|\boldsymbol{x} - \boldsymbol{y}|) \ \mathrm{d}\boldsymbol{y}, \tag{12}$$

where $\boldsymbol{n}$ is the unit normal vector outward from the surface of the particle and $\boldsymbol{n}p$ represents the interfacial pressure at $\mathcal{S}_i$, the surface of particle 'i'. Decomposing the local pressure $p = \overline{p} + p'$, assuming the characteristic size of the filter kernel $\delta_f \gg d_p$ and applying the divergence theorem, the volume filtered pressure gradient can be expressed as

$$\int_{\mathcal{V}_f} \nabla p \mathcal{G}(|\boldsymbol{x} - \boldsymbol{y}|) \ \mathrm{d}\boldsymbol{y} = \nabla (\alpha \overline{p}) - \overline{p} \nabla \alpha - \sum_{i=1}^{N_p} \int_{\mathcal{S}_i} \boldsymbol{n} p' \mathcal{G}(|\boldsymbol{x} - \boldsymbol{y}|) \ \mathrm{d}\boldsymbol{y}, \tag{13}$$

where the last term on the right-hand side of (13) is typically modeled as a contribution to drag. In the context of compressible flows, $\overline{p} \nabla \alpha$ represents a nozzling term that accelerates the gas due to particles restricting the area where fluid can flow [25]. In low-Mach number flows, it is common to simplify the momentum equation by employing the product rule, i.e., $\nabla(\alpha \overline{p}) = \overline{p} \nabla \alpha + \alpha \nabla \overline{p}$, such that the non-conservative nozzeling term $\overline{p} \nabla \alpha$ cancels out. As pointed out by Houim and Oran [25], the product rule is not valid when dealing with compressible flows in general. However, assuming the particle phase is incompressible (i.e., the particle density is not a function of fluid pressure), the product rule will hold.

Applying the same procedure to the viscous stress tensor, the volume filtered momentum equation can be expressed as

$$\frac{\partial \alpha \overline{\rho} \widetilde{\boldsymbol{u}}}{\partial t} + \nabla \cdot (\alpha \{ \overline{\rho} \widetilde{\boldsymbol{u}} \otimes \widetilde{\boldsymbol{u}} + \boldsymbol{R}_u \}) = \alpha \nabla \cdot (\overline{\boldsymbol{\tau}} - \overline{p} \mathbb{I}) + \boldsymbol{\mathcal{F}}. \tag{14}$$

In the above expression, the volume filtered stress tensor is

$$\overline{\boldsymbol{\tau}} = \frac{\widetilde{\mu}}{\mathrm{Re}_c} \left(\nabla \widetilde{\boldsymbol{u}} + \nabla \widetilde{\boldsymbol{u}}^{\mathsf{T}} \right) + \frac{\widetilde{\lambda}}{\mathrm{Re}_c} \nabla \cdot \widetilde{\boldsymbol{u}} + \boldsymbol{R}_\mu, \tag{15}$$

where the sub-filtered flux $\boldsymbol{R}_\mu$ is sometimes modeled as an effective viscosity (e.g., [18, 42, 69]). In addition, $\boldsymbol{\mathcal{F}}$ is the sub-filtered momentum exchange term expressed as

$$\boldsymbol{\mathcal{F}} = \sum_{i=1}^{N_p} \int_{\mathcal{S}_i} \boldsymbol{n} \cdot (p'\mathbb{I} - \boldsymbol{\tau}')\, \mathcal{G}(|\boldsymbol{x} - \boldsymbol{y}|)\ \mathrm{d}\boldsymbol{y}. \tag{16}$$

Finally, $\boldsymbol{R}_u$ is an unresolved stress that arises from filtering the non-linear convective term. This term is usually referred to as a pseudo-turbulent Reynolds stress [33] and is defined as

$$\boldsymbol{R}_u = \overline{\rho} \left(\widetilde{\boldsymbol{u} \otimes \boldsymbol{u}} - \widetilde{\boldsymbol{u}} \otimes \widetilde{\boldsymbol{u}} \right). \tag{17}$$

While this term is typically neglected in incompressible flow models, recent work has shown that these unresolved velocity fluctuations can contribute to a significant portion of the total kinetic energy during particle-shock interactions [24, 35, 48].

2.3.3. Filtered energy

Turning our attention now to the gas-phase energy equation (3), volume filtering the microscale heat flux yields

$$\int_{\mathcal{V}_f} \nabla \cdot \boldsymbol{q} \mathcal{G}(|\boldsymbol{x} - \boldsymbol{y}|)\ \mathrm{d}\boldsymbol{y} = \nabla \cdot (\alpha \overline{\boldsymbol{q}}) - \sum_{i=1}^{N_p} \int_{\mathcal{S}_i} \boldsymbol{n} \cdot \boldsymbol{q} \mathcal{G}(|\boldsymbol{x} - \boldsymbol{y}|)\ \mathrm{d}\boldsymbol{y}. \tag{18}$$

Decomposing the microscale heat flux into $\boldsymbol{q} = \overline{\boldsymbol{q}} + \boldsymbol{q}'$ and rearranging yields

$$\int_{\mathcal{V}_f} \nabla \cdot \boldsymbol{q} \mathcal{G}(|\boldsymbol{x} - \boldsymbol{y}|)\, \mathrm{d}\boldsymbol{y} = \alpha \nabla \cdot \overline{\boldsymbol{q}} - \mathcal{Q}, \tag{19}$$

where $\mathcal{Q}$ accounts for sub-filtered heat transfer at the particle surface typically modeled using a Nusselt number correlation (e.g., [20, 52]), defined as

$$\mathcal{Q} = \sum_{i=1}^{N_p} \int_{\mathcal{S}_i} \boldsymbol{n} \cdot \boldsymbol{q}' \mathcal{G}(|\boldsymbol{x} - \boldsymbol{y}|)\ \mathrm{d}\boldsymbol{y}. \tag{20}$$

and the volume filtered heat flux is

$$\overline{\boldsymbol{q}} = \frac{\widetilde{\mu}}{\mathrm{Re}_c \mathrm{Pr}} \nabla \widetilde{T} + \boldsymbol{R}_q. \tag{21}$$

Similar to the sub-filtered viscous stress tensor appearing in (15), in low-Mach number formulations $\boldsymbol{R}_q$ is sometimes modeled as an effective thermal conductivity to account for enhanced heat dissipation at the particle scale [11, 21, 53].

Volume filtering the work due to pressure in (3) yields

$$\int_{\mathcal{V}_f} \nabla \cdot (p\boldsymbol{u}) \mathcal{G}(|\boldsymbol{x} - \boldsymbol{y}|)\ \mathrm{d}\boldsymbol{y} = \nabla \cdot (\alpha \overline{p\boldsymbol{u}}) - \sum_{i=1}^{N_p} \int_{\mathcal{S}_i} \boldsymbol{n} \cdot (p\boldsymbol{u}) \mathcal{G}(|\boldsymbol{x} - \boldsymbol{y}|)\ \mathrm{d}\boldsymbol{y}. \tag{22}$$

In this expression, $\overline{p\boldsymbol{u}}$ contains the product between sub-filtered pressure and velocity fluctuations, which will be combined with additional sub-filtered terms to form $\boldsymbol{R}_{Tu}$ later. Similarly, volume filtering the work due to viscous stresses in (3) yields

$$\begin{aligned} -\int_{\mathcal{V}_f} \nabla \cdot (\boldsymbol{u} \cdot \boldsymbol{\tau}) \mathcal{G}(|\boldsymbol{x} - \boldsymbol{y}|)\ \mathrm{d}\boldsymbol{y} &= -\nabla \cdot (\alpha \widetilde{\boldsymbol{u}} \cdot \overline{\boldsymbol{\tau}}) - \nabla \cdot (\alpha \boldsymbol{R}_{\tau u}) \\ &\quad + \sum_{i=1}^{N_p} \int_{\mathcal{S}_i} \boldsymbol{n} \cdot (\boldsymbol{u} \cdot \boldsymbol{\tau}) \mathcal{G}(|\boldsymbol{x} - \boldsymbol{y}|)\ \mathrm{d}\boldsymbol{y}, \end{aligned} \tag{23}$$

where $\boldsymbol{R}_{\tau u} = \overline{\boldsymbol{u}\cdot\boldsymbol{\tau}} - \widetilde{\boldsymbol{u}}\cdot\overline{\boldsymbol{\tau}}$, which is unclosed and represents work due to the sub-filtered viscous stress.

We emphasize here that the surface contributions on the right-hand side of Eqs. (22) and (23) must be treated with care. Unlike in the momentum equation, the presence of the gas-phase velocity in the sub-filtered stresses results in additional cross-terms when decomposing the variables. These cross-terms can be treated in a variety of ways, and the choice will have a direct consequence on how the unclosed terms should be interpreted. Focusing on the pressure work term $\sum_i \int_{\mathcal{S}_i} \boldsymbol{n}\cdot(p\boldsymbol{u})\mathcal{G}(|\boldsymbol{x}-\boldsymbol{y}|)\ \mathrm{d}\boldsymbol{y}$, we highlight two approaches that can be taken:

1. Enforcing a no-slip condition at the particle surface, the fluid-phase velocity can be decomposed into $\boldsymbol{u}\big|_{\mathcal{S}_i} = \boldsymbol{v}_p^{(i)} + \dot{r}_p^{(i)}\boldsymbol{n}$, where $\boldsymbol{v}_p^{(i)}$ is the velocity of particle 'i' and $\dot{r}_p^{(i)}$ is the rate of change of its radius. Decomposing pressure into its filtered and sub-filtered contributions, and assuming rigid particles (i.e., $\dot{r}_p = 0$), the last term on the right-hand side of (22) becomes

$$\begin{aligned}-\sum_{i=1}^{N_p}\int_{\mathcal{S}_i}\boldsymbol{n}\cdot(p\boldsymbol{u})\mathcal{G}(|\boldsymbol{x}-\boldsymbol{y}|)\ \mathrm{d}\boldsymbol{y} = -\overline{p}\sum_{i=1}^{N_p}\int_{\mathcal{S}_i}\boldsymbol{n}\cdot\boldsymbol{v}_p^{(i)}\mathcal{G}(|\boldsymbol{x}-\boldsymbol{y}|)\ \mathrm{d}\boldsymbol{y}\\ -\sum_{i=1}^{N_p}\int_{\mathcal{S}_i}\boldsymbol{n}\cdot\left(p'\boldsymbol{v}_p^{(i)}\right)\mathcal{G}(|\boldsymbol{x}-\boldsymbol{y}|)\ \mathrm{d}\boldsymbol{y}.\end{aligned} \tag{24}$$

Applying Leibniz rule on the first term on the right-hand side of Eq. (24) and recognizing that $\boldsymbol{v}_p$ is uniform across the volume of each particle, Eq. (24) can be rewritten as

$$\begin{aligned}-\sum_{i=1}^{N_p}\int_{\mathcal{S}_i}\boldsymbol{n}\cdot(p\boldsymbol{u})\mathcal{G}(|\boldsymbol{x}-\boldsymbol{y}|)\ \mathrm{d}\boldsymbol{y} = \overline{p}\nabla\cdot(\alpha_p\boldsymbol{u}_p)\\ -\sum_{i=1}^{N_p}\boldsymbol{v}_p^{(i)}\cdot\int_{\mathcal{S}_i}p'\boldsymbol{n}\mathcal{G}(|\boldsymbol{x}-\boldsymbol{y}|)\ \mathrm{d}\boldsymbol{y},\end{aligned} \tag{25}$$

where $\boldsymbol{u}_p$ is a filtered (Eulerian) representation of the particle-phase velocity that can be obtained via

$$\alpha_p\boldsymbol{u}_p = \sum_{i=1}^{N_p}\boldsymbol{v}_p^{(i)}\mathcal{G}\left(|\boldsymbol{x}-\boldsymbol{x}_p^{(i)}|\right)\mathcal{V}_p. \tag{26}$$

As discussed by Houim and Oran [25], assuming constant particle density the disperse phase continuity equation can be employed to yield

$$\overline{p}\nabla\cdot(\alpha_p\boldsymbol{u}_p) = -\overline{p}\frac{\partial\alpha_p}{\partial t} = \overline{p}\frac{\partial\alpha}{\partial t}, \tag{27}$$

where $\overline{p}\partial\alpha/\partial t$ represents a pDV work term due to particles entering or leaving a control volume. While the first term on the right-hand side of Eq. (25) and the expression above are equivalent, expressing this in terms of volume fraction gradients, as is done in Eq. (25), may be more convenient numerically. It is interesting to note that Houim and Oran [25] arrived at this term via a control volume analysis, in which an 'interfacial pressure' was used at the particle surface and for closure assumed this to be equal to the local gas-phase pressure. Meanwhile, the pDV work

term naturally appears through volume filtering, and we show that the pressure used is indeed the local gas-phase pressure.

A similar approach can be applied to the viscous work term, which yields

$$\int_{\mathcal{V}} \nabla \cdot (\boldsymbol{u} \cdot \boldsymbol{\tau}) \mathcal{G}(|\boldsymbol{x}-\boldsymbol{y}|)\ \mathrm{d}\boldsymbol{y} = \nabla \cdot (\alpha \widetilde{\boldsymbol{u}} \cdot \overline{\boldsymbol{\tau}}) + \nabla \cdot (\alpha \boldsymbol{R}_{\tau u}) + \overline{\boldsymbol{\tau}} : \nabla (\alpha_p \boldsymbol{u}_p) - \sum_{i=1}^{N_p} \int_{\mathcal{S}_i} \boldsymbol{n} \cdot \left(\boldsymbol{v}_p^{(i)} \cdot \boldsymbol{\tau}'\right) \mathcal{G}(|\boldsymbol{x}-\boldsymbol{y}|)\ \mathrm{d}\boldsymbol{y}, \tag{28}$$

It is important to note that the last term in Eqs. (25) and (28) represents the same unclosed term that appeared in Sec. 2.3.2 typically modeled as drag, except multiplied by the particle velocity, which can be rewritten as $\boldsymbol{u}_p \cdot \boldsymbol{\mathcal{F}}$.

2. Alternatively, if the fluid-phase velocity is not replaced by the particle velocity in the last term on the right-hand side of (22), pressure and velocity can respectively be split into filtered and sub-filtered components as

$$-\sum_{i=1}^{N_p} \int_{\mathcal{S}_i} \boldsymbol{n} \cdot (p\boldsymbol{u}) \mathcal{G}(|\boldsymbol{x}-\boldsymbol{y}|)\ \mathrm{d}\boldsymbol{y} = -\sum_{i=1}^{N_p} \int_{\mathcal{S}_i} \boldsymbol{n} \cdot (\overline{p}\ \widetilde{\boldsymbol{u}} + \overline{p}\boldsymbol{u}'' + p'\widetilde{\boldsymbol{u}} + p'\boldsymbol{u}'') \mathcal{G}(|\boldsymbol{x}-\boldsymbol{y}|)\ \mathrm{d}\boldsymbol{y}. \tag{29}$$

Once again, a similar approach can be applied to the viscous work term. It can immediately be seen that this approach results in different closure terms, none of which resemble $\boldsymbol{\mathcal{F}}$ that appears in Eq. (14).

In summary, different choices can be made when volume filtering the pressure and viscous work terms in the energy equation. While both are correct, they require different closure. Here we employ Approach 1 as it leads to fewer unclosed terms. Applying Approach 1 and filtering the remaining terms yields

$$\frac{\partial \alpha \overline{\rho} \widetilde{E}}{\partial t} + \nabla \cdot \left(\alpha \overline{\rho} \widetilde{E} \widetilde{\boldsymbol{u}}\right) + \nabla \cdot (\alpha(\overline{p}\widetilde{\boldsymbol{u}} - \widetilde{\boldsymbol{u}} \cdot \overline{\boldsymbol{\tau}})) + \alpha \nabla \cdot \overline{\boldsymbol{q}} = -(\overline{p}\mathbb{I} - \overline{\boldsymbol{\tau}}) : \nabla (\alpha_p \boldsymbol{u}_p) + \boldsymbol{u}_p \cdot \boldsymbol{\mathcal{F}} + \mathcal{Q} - \nabla \cdot \left(\alpha \{\boldsymbol{R}_{Tu} + \frac{1}{2}\boldsymbol{R}_{uu} - \boldsymbol{R}_{\tau u}\}\right), \tag{30}$$

which leads to a number of unclosed terms that are often neglected, such as the pseudo-turbulent diffusion $\boldsymbol{R}_{uu} = \overline{\rho}\left(\widetilde{\boldsymbol{u} \cdot \boldsymbol{u} \otimes \boldsymbol{u}} - \widetilde{\boldsymbol{u} \cdot \boldsymbol{u}} \otimes \widetilde{\boldsymbol{u}}\right)$, pseudo-turbulent heat flux $\boldsymbol{R}_{Tu} = \overline{\rho}\left(\widetilde{T\boldsymbol{u}} - \widetilde{T}\,\widetilde{\boldsymbol{u}}\right)$, and work due to sub-filtered viscous stresses, $\boldsymbol{R}_{\tau u}$. The work due to momentum exchange is defined as

$$\boldsymbol{u}_p \cdot \boldsymbol{\mathcal{F}} = \sum_{i=1}^{N_p} \boldsymbol{v}_p^{(i)} \cdot \int_{\mathcal{S}_i} \boldsymbol{n} \cdot (p'\mathbb{I} - \boldsymbol{\tau}')\, \mathcal{G}(|\boldsymbol{x}-\boldsymbol{y}|)\ \mathrm{d}\boldsymbol{y}. \tag{31}$$

It should be noted that $\widetilde{\boldsymbol{u}} \cdot \boldsymbol{\mathcal{F}}$ is sometimes employed as the work due to drag [29, 68], which was obtained by keeping the fluid velocity at the particle surface instead of decomposing it into $\boldsymbol{u}\big|_{\mathcal{S}_i} = \boldsymbol{v}_p^{(i)} + \dot{r}_p^{(i)}\boldsymbol{n}$. As shown in Approach 2, this procedure introduces additional terms that contain products of filtered and sub-filtered stresses with the fluid velocity, which are not properly accounted for by $\boldsymbol{\mathcal{F}}$. An alternative argument for the proper form of the work due to interphase exchange is presented in Ling et al. [28] where it is shown that $\boldsymbol{u}_p \cdot \boldsymbol{\mathcal{F}}$ must be used due to energy arguments.

2.3.4. Filtered equation of state

The filtered equation of state is given by

$$\widetilde{T} = \frac{\gamma \overline{p}}{(\gamma - 1)\overline{\rho}}, \tag{32}$$

which does not result in any residual contributions if the Favre-filtered temperature is used in the filtered heat flux (21). Filtering the thermodynamic relation between pressure and energy results in

$$\overline{p} = (\gamma - 1)\left(\overline{\rho}\widetilde{E} - \frac{1}{2}\overline{\rho}\widetilde{\boldsymbol{u}} \cdot \widetilde{\boldsymbol{u}} - \overline{\rho}k\right). \tag{33}$$

In this expression, $\overline{\rho}k = \mathrm{tr}\left(\boldsymbol{R}_u\right)/2$ where k is the pseudo-turbulent kinetic energy (PTKE). It can immediately be seen that k systematically acts to reduce the local pressure. As a consequence, neglecting this term could lead to underpredictions of the local Mach number. The role of PTKE on local Mach number will be analyzed in Sec. 3.5.

2.3.5. Transport of PTKE

To help guide model development in later sections, a transport equation is derived for the PTKE. Differentiating $\alpha\overline{\rho}k = \alpha\overline{\rho}\left(\widetilde{\boldsymbol{u}\cdot\boldsymbol{u}} - \widetilde{\boldsymbol{u}}\cdot\widetilde{\boldsymbol{u}}\right)/2$ in time, applying the same filtering procedure from prior sections and rearranging terms yields

$$\begin{aligned}\frac{\partial \alpha\overline{\rho}k}{\partial t} + \nabla\cdot\left(\alpha\overline{\rho}\widetilde{\boldsymbol{u}}k\right) + \frac{1}{2}\nabla\cdot\left(\alpha\boldsymbol{R}_{uu}\right) - \widetilde{\boldsymbol{u}}\cdot\nabla\cdot\left(\alpha\boldsymbol{R}_u\right) = \\ -\left(\overline{p}\mathbb{I} - \overline{\boldsymbol{\tau}}\right):\nabla\left(\alpha\widetilde{\boldsymbol{u}} + \alpha_p\boldsymbol{u}_p\right) + \left(\boldsymbol{u}_p - \widetilde{\boldsymbol{u}}\right)\cdot\boldsymbol{\mathcal{F}} \\ -\nabla\cdot\alpha\left(\boldsymbol{R}_{pu} - \boldsymbol{R}_{\tau u}\right) - \alpha\overline{p\nabla\cdot\boldsymbol{u}} + \alpha\overline{\boldsymbol{\tau}:\nabla\boldsymbol{u}}.\end{aligned} \tag{34}$$

In the expression above, the first line represents transport of PTKE. Except for the term containing $\boldsymbol{\mathcal{F}}$, the second line contains terms that are closed, i.e. they are entirely expressed in terms of volume-filtered quantities. The last line contains unclosed (sub-filtered) contributions, such as $\boldsymbol{R}_{pu}$ that involves fluctuations of sub-filtered velocity and pressure, that contributes to pressure diffusion. $\left(\boldsymbol{u}_p - \widetilde{\boldsymbol{u}}\right)\cdot\boldsymbol{\mathcal{F}}$ is a source term that acts to produce PTKE. Note that if k is omitted from the pressure relation (33) (as is typically done), the interphase source terms that contribute to PTKE would appear in the transport equation for the gas-phase pressure (see [7] for details). A model to close the transported PTKE will be proposed in later sections.

2.3.6. A summary of unclosed terms

The volume filtered conservation equations lead to a number of sub-filtered terms and the so-called "closure problem". In summary, the unclosed terms can be grouped into residual stresses $\boldsymbol{R}_u$ in Eqs. (14) and (33), $\boldsymbol{R}_\mu$ in Eq. (15), $\boldsymbol{R}_{Tu}$, $\boldsymbol{R}_{uu}$, and $\boldsymbol{R}_{\tau u}$ in Eq. (30), $\boldsymbol{R}_q$, in Eq. (21), and $\boldsymbol{R}_{pu}$ in Eq. (34). In addition, a number of sub-filtered surface contributions appear in the form of interphase exchange terms, including the interphase exchange of momentum, $\boldsymbol{\mathcal{F}}$, in Eq. (14), as well as work due to momentum exchange, $\boldsymbol{u}_p\cdot\boldsymbol{\mathcal{F}}$, and heat exchange, $\mathcal{Q}$, in Eq. (30). Closure models have been proposed for some of these terms, such as drag (e.g., [19, 41, 58] to name a few) and heat exchange [20, 59], but for most part are only valid in the incompressible limit and therefore are likely not applicable to the current study. It is important to note that the unclosed stresses are analogous to those that appear in single-phase large-eddy simulations (LES), but physically represent substantially different effects. In both the present volume-filtered

formulation and in LES, large scale structures are resolved while small scale structures require models. That being said, the classification "LES" should not be used lightly as it traditionally applies to cases where there exists an energy cascade. Moreover, these terms can be non-negligible even in laminar flows (e.g., via steady wakes), and thus the use of single-phase closure for the terms summarized above should be done with utmost care. The relative contribution of these unclosed terms will be evaluated in later sections using particle-resolved DNS.

3. *A posteriori* analysis

In this section, we evaluate the relative contributions of the unclosed terms appearing in Sec. 2.3 by spatially filtering a direct solution to the microscale equations. Numerical simulations of the shock-particle configuration illustrated in Fig. 1 are first presented, followed by an *a posteriori* analysis consistent with the filtering operators introduced in Sec. 2.2. Details on filtering methodology are provided in Appendix A. We briefly note that while the present analysis considers collections of monodisperse particles, the same filtering approach can be extended to polydisperse suspensions. In practice, the filter size applied to flows with polydisperse particles is typically chosen to be larger than the maximum particle size (e.g., [5, 9].)

3.1. Simulation configuration

The simulations are designed to emulate the multiphase shock tube experiment of Wagner et al. [66] and numerous computational studies since then [24, 29, 45, 61]. A shock wave passes through a suspension of rigid spherical particles distributed over a thickness $L^\star = 2$ mm (as shown in Fig. 2). The domain size is $L_x = 7.5$ in the streamwise direction, and $L_y = 1$ in the spanwise direction. All length scales are non-dimensionalized by $L^\star$. The shock is initialized at $x = 2.4$ with a shock Mach number of $\mathrm{Ma}_s = 1.66$. The post-shock (denoted with a subscript '1') and pre-shock (denoted with a subscript '2') conditions are given by $(\rho_1,\ p_1,\ u_1 \mid \rho_2,\ p_2,\ u_2) = (2.131,\ 2.177,\ 0.881 \mid 1,\ 0.714,\ 0)$. The Reynolds number based on $L^\star$ and the sound speed $c^\star_\infty = 343$ m/s is $\mathrm{Re}_c = 45394$.

Particles have density $\rho_p = 2520$ (non-dimensionalized by the gas-phase density) and diameter $d_p = 0.0575$, corresponding to 115 μm soda lime particles in air. A uniform grid of size 5250×700 is employed such that there are approximately 40 grid points across the diameter of each particle. Particles are initially distributed within a length of $L = 1$ starting at $x_0 = 2.5$ with a mean volume fraction within the span of $\varphi_p = 0.04$, 0.21, and 0.44, corresponding to $N_p = 16$, 81, and 169 particles, respectively. For the distribution, particles are initially placed uniformly and then every other column is shifted vertically by a distance equal to one half the mean inter-particle spacing $\lambda_p/2$. This creates a staggered arrangement of particles. Each particle is then randomly perturbed within a radius less than $(\lambda_p - d_p)/2$ to mimic a random distribution while avoiding overlap with neighbors.

In this section, we consider two-dimensional simulations of stationary particles. With the parameters listed above, the ratio of the non-dimensional particle timescale, $\tau_p = \rho_p d_p^2/(18\mu) \approx 21000$, to the particle acoustic time scale, $\tau_d = d_p/c_\infty = 0.0575$, is large, indicating the particle motion is negligible over the simulation duration considered ($t < 3$). In addition, a recent experimental study suggests that the particle phase does not begin to spread until times corresponding to our non-dimensional time of $t \gtrsim 10$ [14]. Here, $t = 0$ corresponds to the instant the shock interacts with the leading edge of

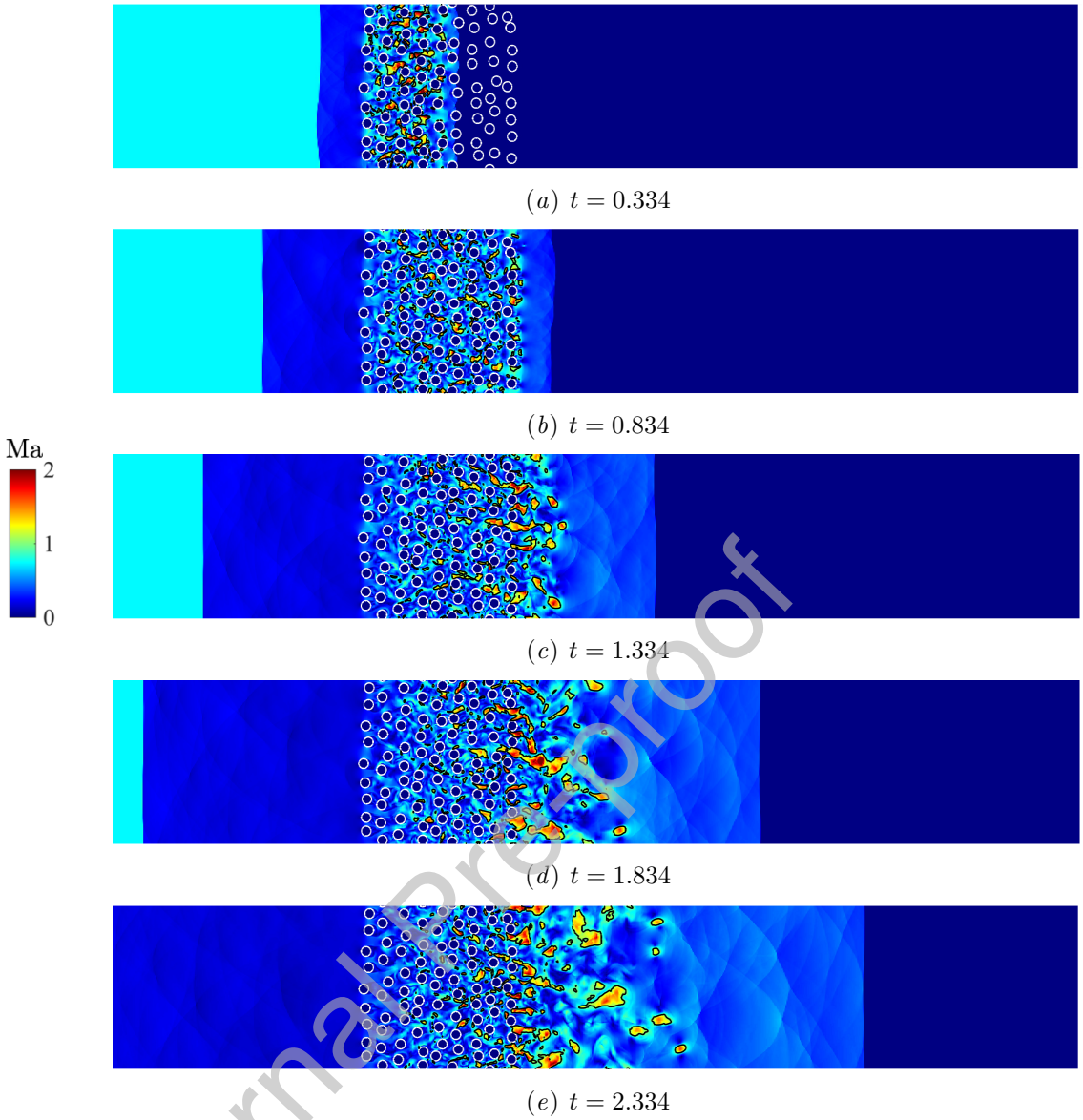

Figure 2: Mach number fields (color) for $\varphi_p = 0.21$. Contours of Ma = 1 (—).

the particle phase. Thus, the assumption of stationary particles is valid over the time durations considered in this *a posteriori* analysis. We briefly note that the dynamics of a shock interacting with a spherical particle in three dimensions and a cylindrical particle in two dimensions are fundamentally different due to the timescales associated with the shock propagation. In addition, the wake structures confined in two dimensions result in larger values of PTKE compared to three dimensional configurations [35]. Despite this, two-dimensional simulations are performed in the present study to avoid the high computational cost associated with a direct solution to the three-dimensional viscous compressible flow equations. Thus, we seek to identify qualitative trends in the sub-filtered terms with mean particle concentration and filter size.

3.2. Discretization of the microscale equations

The microscale equations (1)–(3) are discretized using narrow-stencil high-order finite difference operators that satisfy the summation-by-parts (SBP) property on a structured

curvilinear grid [51, 54]. All simulations presented in this study use the sixth-order formulation in the domain interior, and third-order, one-sided operators at the boundary, resulting in overall fourth-order accuracy for the fluid-phase equations. To evaluate second and mixed derivatives, first derivative operators are applied consecutively, necessitating the use of artificial dissipation to damp the highest wavenumber components supported by the grid. To this end, high-order accurate SBP dissipation operators are used that provide artificial viscosity based on a sixth-order derivative with a diffusion coefficient that is a function of the local grid resolution [31, 65].

The SBP scheme is combined with the simultaneous approximation term (SAT) boundary treatment [10, 55] to ensure energy stability. This is achieved by enforcing non-reflecting characteristic boundary conditions weakly at the far field [55]. In addition, an absorbing sponge region [16] is applied at the domain boundary to prevent unphysical acoustic reflections by adding a damping term to the right-hand side of the fluid-phase equations. Finally, the equations are advanced in time using a standard fourth-order Runge–Kutta method.

Boundary conditions are enforced at the surface of each particle via a direct-forcing immersed boundary method. In this approach, Lagrangian markers are distributed over the surface of each particle and the gas-phase velocity is interpolated to the location of each to generate a forcing term added to the momentum equation (2). The associated work done by the immersed boundary is added to the microscale energy equation (3). A signed distance function is used to penalize the flow at grid points located within the solid phase to avoid spurious reflections as shocks pass through the particles. Additional details on this method can be found in Boukharfane et al. [6], Uhlmann [63].

3.3. Role of filtering on the Mach number

Instantaneous snapshots of the local Mach number for the $\varphi_p = 0.21$ case are shown in Fig. 2. Shortly after the shock interacts with the particles, a reflected shock propagates upstream while a transmitted shock travels through the particle suspension. The particles act to restrict the area of the transmitted shock, causing the gas phase to choke near the downstream edge due to the immediate change in volume fraction, followed by supersonic expansion. This rapid increase in gas-phase velocity at the downstream edge was found to significantly increase the particle acceleration in three-dimensional simulations of freely-evolving shock-particle interactions [61]. As discussed in Theofanous et al. [61], modeling approaches based on spatially averaged fields (e.g., Eulerian–Eulerian and Eulerian–Lagrangian methods) fail to predict this choking behavior, and are thus unable to accurately predict particle dispersion.

To explore this concept further, the local Mach number is shown in Fig. 3(a) computed using filtered quantities according to $\mathrm{Ma} = |\widetilde{\boldsymbol{u}}|/\sqrt{(\gamma-1)\widetilde{T}}$ shortly after the shock has passed through the particle suspension. The flow field obtained from particle-resolved DNS is spatially filtered using the operators defined in Sec. 2.2 for filter sizes ranging between $0 \leq \delta_f \leq 4d_p$. The local volume fraction is also plotted by filtering the indicator function defined in Eq. (8). Details on the implementation of the filtering procedure can be found in Appendix A. Filtering (or locally averaging) the flow field systematically acts to reduce the extent to which the gas phase accelerates at the downstream edge of the particles. In addition, the filter acts to 'smear' the volume fraction, and consequently the nozzle-like flow contraction would be less significant when solving the volume-filtered equations. Here, we argue that with proper treatment of the sub-filtered terms, the correct level of particle acceleration can be recovered.

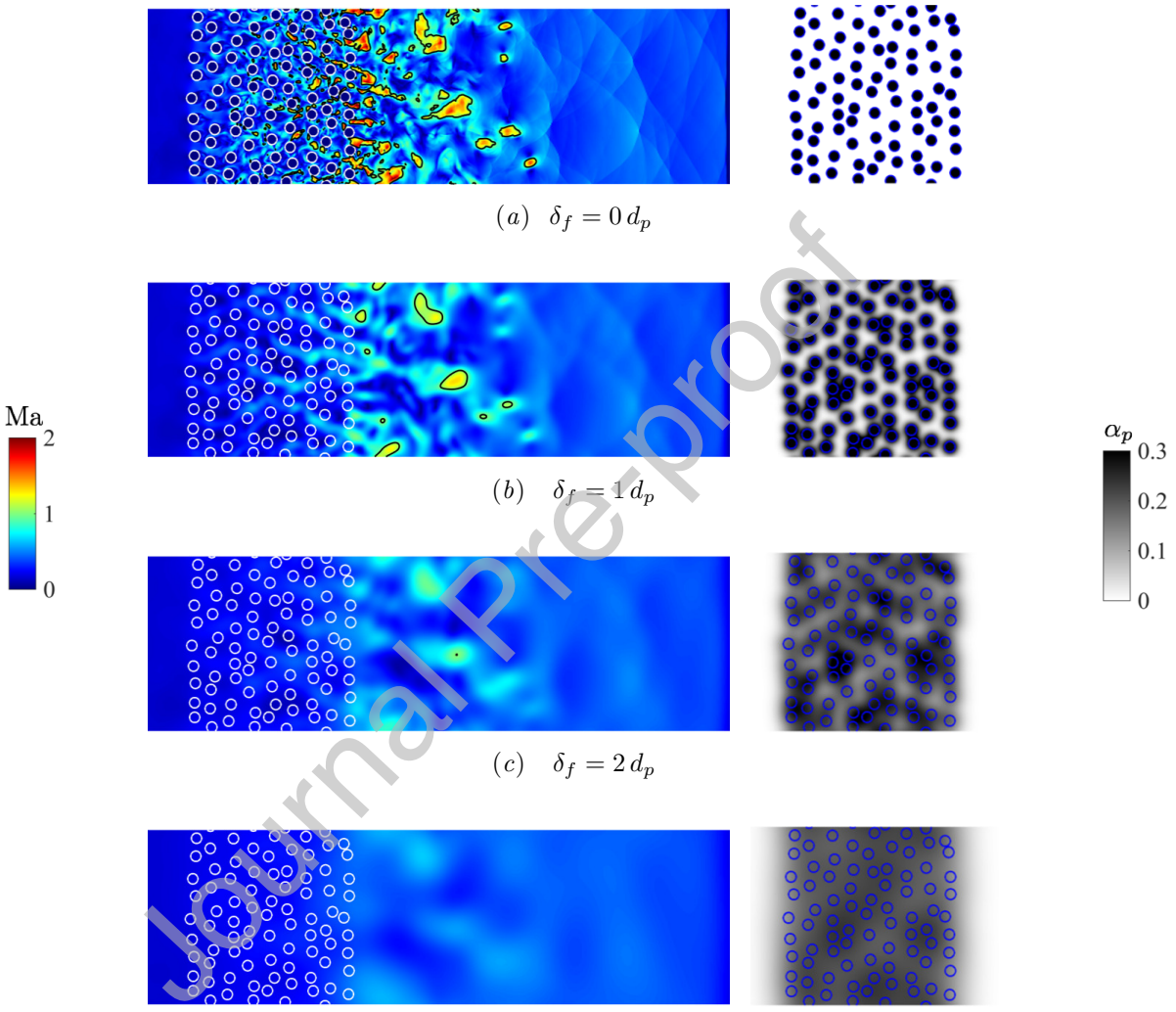

Figure 3: Mach number (left) and particle volume fraction (right) as a function of filter size for $\varphi_p = 0.21$ when $t = 2.334$. Contours of Ma $= 1$ (—).

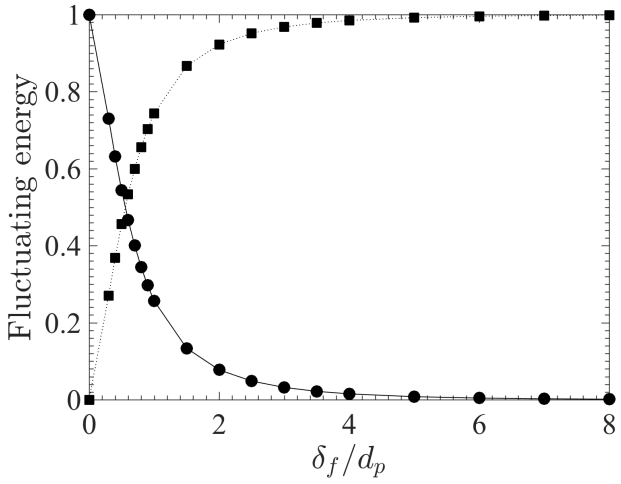

Figure 4: Relative contributions of the fluctuating kinetic energy averaged across the entire domain. Filtered fluctuations, $\langle \widetilde{\boldsymbol{u}} \cdot \widetilde{\boldsymbol{u}} \rangle_{xy} - \langle \widetilde{\boldsymbol{u}} \rangle_{xy} \cdot \langle \widetilde{\boldsymbol{u}} \rangle_{xy}$ (–●–), and sub-filtered fluctuations, $\langle \boldsymbol{u} \cdot \boldsymbol{u} \rangle_{xy} - \langle \widetilde{\boldsymbol{u}} \cdot \widetilde{\boldsymbol{u}} \rangle_{xy}$ (··■··), as a function of filter size for $\varphi_p = 0.21$ when $t = 2.334$, normalized by the total fluctuating energy.

3.4. Role of filtering on the velocity fluctuations

As shown in Sec. 2, one consequence of volume filtering is the appearance of sub-filtered velocity fluctuations in the Reynolds stress-like term $\boldsymbol{R}_u$, pseudo-turbulent diffusion $\boldsymbol{R}_{uu}$, and PTKE k. From Fig. 3, it can be seen that the majority of the velocity fluctuations contained in the filtered field are suppressed when $\delta_f \gtrapprox 4d_p$. To quantify the relative contributions of the filtered and sub-filtered fluctuations, the velocity field is decomposed into $\boldsymbol{u} = \widetilde{\boldsymbol{u}} + \boldsymbol{u}''$, and then averaged across the x- (streamwise) and y- (spanwise) directions. In this work, angled brackets denote Favre averaging, and the subscript denotes the direction in which averaging is performed. For example, averaging across y is given by $\langle A \rangle_y = \int_0^{L_y} (\alpha \overline{\rho} A) \ \mathrm{d}y / \int_0^{L_y} (\alpha \overline{\rho}) \ \mathrm{d}y$, for an arbitrary quantity A. With this, the domain-average filtered velocity is defined as $\langle \widetilde{\boldsymbol{u}} \rangle_{xy}$, which can be used to construct the total fluctuating kinetic energy as $\langle \boldsymbol{u} \cdot \boldsymbol{u} \rangle_{xy} - \langle \widetilde{\boldsymbol{u}} \rangle_{xy} \cdot \langle \widetilde{\boldsymbol{u}} \rangle_{xy}$. The portion of this energy containing only filtered terms is $\langle \widetilde{\boldsymbol{u}} \cdot \widetilde{\boldsymbol{u}} \rangle_{xy} - \langle \widetilde{\boldsymbol{u}} \rangle_{xy} \cdot \langle \widetilde{\boldsymbol{u}} \rangle_{xy}$, and the residual contributions contain only sub-filtered terms, i.e. $\langle \boldsymbol{u} \cdot \boldsymbol{u} \rangle_{xy} - \langle \widetilde{\boldsymbol{u}} \cdot \widetilde{\boldsymbol{u}} \rangle_{xy}$. In the limit $\delta_f \to \infty$, $\widetilde{\boldsymbol{u}} \to \langle \widetilde{\boldsymbol{u}} \rangle_{xy}$, and all of the fluctuations reside at the sub-filter scale.

As seen in Fig. 4, the filtered and sub-filtered components of the fluctuating energy have equal contributions when $\delta_f \approx d_p$, and the majority of energy resides at the sub-filter scale when $\delta_f \gtrapprox 4d_p$. In practice, the gas phase is typically discretized on a mesh with grid spacing larger than the particle diameter. If δ_f is interpreted as the grid spacing, this would suggest the subgrid-scale velocity fluctuations always contribute significantly to the total fluctuating kinetic energy. In addition, any model for the subgrid-scale velocity fluctuations under these conditions should be aware of the portion of energy being resolved when δ_f is not significantly larger than the particle diameter.

Figure 5 shows streamwise profiles of the averaged PTKE as a function of filter size and mean particle volume fraction. The PTKE obtained using sub-filtered velocity fluctuations is compared to the result obtained from ensemble averaging the microscale velocity in the y-direction. Ensemble averaging is typically employed when extracting statistics from particle-resolved simulations of similar configurations [24, 35, 39, 45]. Except for the most dilute case ($\varphi_p = 0.04$), PTKE obtained from ensemble averaging exhibits qual-

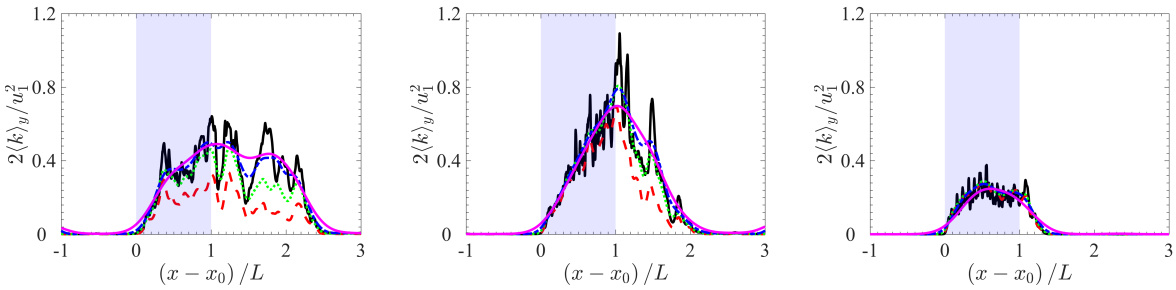

(a) $\varphi_p = 0.04$ (b) $\varphi_p = 0.21$ (c) $\varphi_p = 0.44$

Figure 5: Comparison of PTKE obtained from ensemble averaging (—) and volume filtering with $\delta_f = d_p$ (- - -), $\delta_f = 2d_p$ (·····), $\delta_f = 4d_p$ (-·-·-), and $\delta_f = 8d_p$ (—) at $t = 2.334$. The shaded region (▒) indicates particle location.

itatively similar trends. For the most dilute case, the magnitude of PTKE increases as the filter size increases, approaching the solution obtained from ensemble averaging when $\delta_f \gtrapprox 4d_p$. For each case, PTKE based on ensemble averaging is significantly more noisy than its filtered counterpart due to the lack of averaging in the x-direction.

In general, PTKE is seen to depend on both δ_f and φ_p. A key trend observed in Fig. 5 is that the PTKE dependence on δ_f only occurs when the volume fraction is sufficiently small. The simulation results reveal that the PTKE dependence can be collapsed to a Knudsen number based on the mean inter-particle spacing, λ_p, given by

$$\mathrm{Kn}_\delta = \frac{\lambda_p}{\delta_f}. \tag{35}$$

When $\mathrm{Kn}_\delta < 1$, the majority of the velocity fluctuations generated in particle interstitial sites reside within the support of the filter kernel. As seen in Fig. 6, the cases with $\varphi_p = 0.21$ and 0.44 correspond to $\mathrm{Kn}_\delta < 1$, and thus PTKE is not seen to vary with δ_f in Figs. 5(b)–5(c). When $\delta_f = d_p$, $\mathrm{Kn}_\delta > 1$ across all possible volume fractions (dilute to close-packing). In summary, models attempting to predict PTKE need not take into consideration both the local volume fraction and filter size, but instead this dependency can be captured via Kn_δ. For freely-evolving particle suspensions, Kn_δ will vary in space and time.

3.5. Assessment of the unclosed terms

The magnitude of the unclosed stresses appearing in the volume-filtered energy equation (30) are provided in Fig. 7 for $\delta_f = d_p$ and $4d_p$ and compared against the resolved (filtered) pressure work term $\overline{p}\widetilde{\boldsymbol{u}}$. The larger filter size acts to smooth out the profiles, without noticeable change to their magnitude. Owing to the effect of Kn_δ as previously discussed, the dependence of the sub-filtered stresses on δ_f is only seen for the most dilute case. Perhaps not unexpectedly, the sub-filtered correlation between the viscous stress and velocity, $\boldsymbol{R}_{\tau u}$, is negligible owing to the large Reynolds numbers under consideration. The pseudo-turbulent heat flux, $\boldsymbol{R}_{Tu}$, is also relatively small. The pseudo-turbulent diffusion, $\boldsymbol{R}_{uu}$, is seen to be the dominating sub-filtered stress. This term contains triple products of sub-filtered velocity fluctuations, which could be challenging to develop models for. This term is sometimes expressed as a product of the filtered velocity and Reynolds stress. It can be seen in Fig. 7 that $\boldsymbol{R}_{uu} \approx 2\boldsymbol{R}_u \cdot \widetilde{\boldsymbol{u}}$ yields overall good agreement. In summary, $\boldsymbol{R}_{uu}$ is the only non-negligible sub-filtered stress appearing in Eq. (30), which can be closed provided a model for $\boldsymbol{R}_u$.

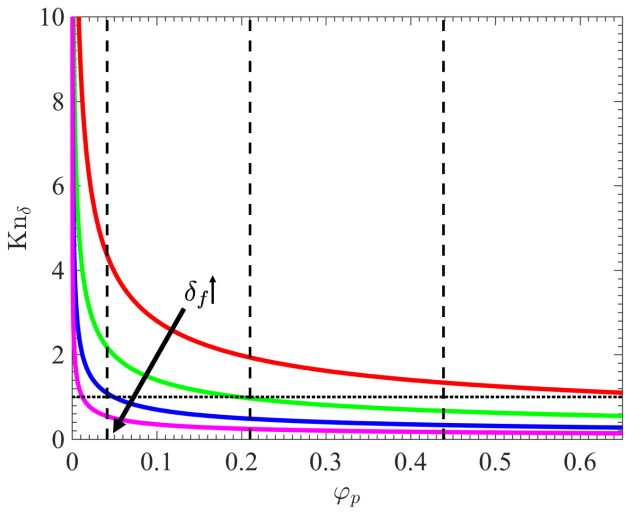

Figure 6: Filter size dependent Knudsen number as a function of φ_p with $\delta_f = d_p$, (—), $\delta_f = 2d_p$ (—), $\delta_f = 4d_p$ (—), and $\delta_f = 8d_p$ (—). Reference lines are also shown for $\mathrm{Kn}_\delta = 1$ ($\cdots$) and the three volume fractions under consideration (- - -).

In Sec. 2.3.4, we showed that filtering the equation of state results in an additional contribution by the PTKE when computing pressure. From Eq. (33), it can be seen that the PTKE systematically acts to reduce the local pressure, which could result in underpredictions of the local Mach number if not accounted for properly. This could be especially important in regions of large volume fraction gradients that were demonstrated to choke the flow and lead to supersonic expansion. To quantify this error, we compare the pressure obtained using only filtered quantities (i.e., neglecting PTKE), as is typically done in coarse-grained simulations of gas-solid flows, with the true filtered pressure that contains this contribution. From Fig. 8, it can be seen that errors in the pressure field are maximum near the downstream edge of the particle suspension where the gas phase accelerates to supersonic speeds. As much as 25% discrepancy is observed in the pressure field when neglecting PTKE with $\delta_f = d_p$. The maximum local error is not as significant for $\delta_f = 4d_p$, but still results in approximately 15% relative error. Because $\mathrm{Ma} \propto \sqrt{\overline{p}}$, the errors in Mach number are even more significant.

4. Coarse-grained modeling

In this section, we present a volume-filtered Eulerian–Lagrangian (VF-EL) approach for simulating compressible particle-laden flows. First, a model is proposed for transporting PTKE and reconstructing the pseudo-turbulent Reynolds stress tensor. Details on the numerical discretization of the volume-filtered equations are then presented, followed by verification and validation against existing data. For clarity of presentation, the $\overline{(\cdot)}$ and $\widetilde{(\cdot)}$ notation will be dropped in the remainder of the paper.

4.1. Modeling PTKE and the pseudo-turbulent Reynolds stresses

The *a posteriori* analysis performed in Sec. 3 demonstrated the PKTE, k, in compressible gas-solid flows. While algebraic models for this term have been proposed in the past [33, 39], a key feature of pseudo-turbulence in the flows considered here is that it gets advected with the mean flow downstream from the particles (see Fig. 5). Therefore, models for k based on the local volume fraction will fail to accurately predict important

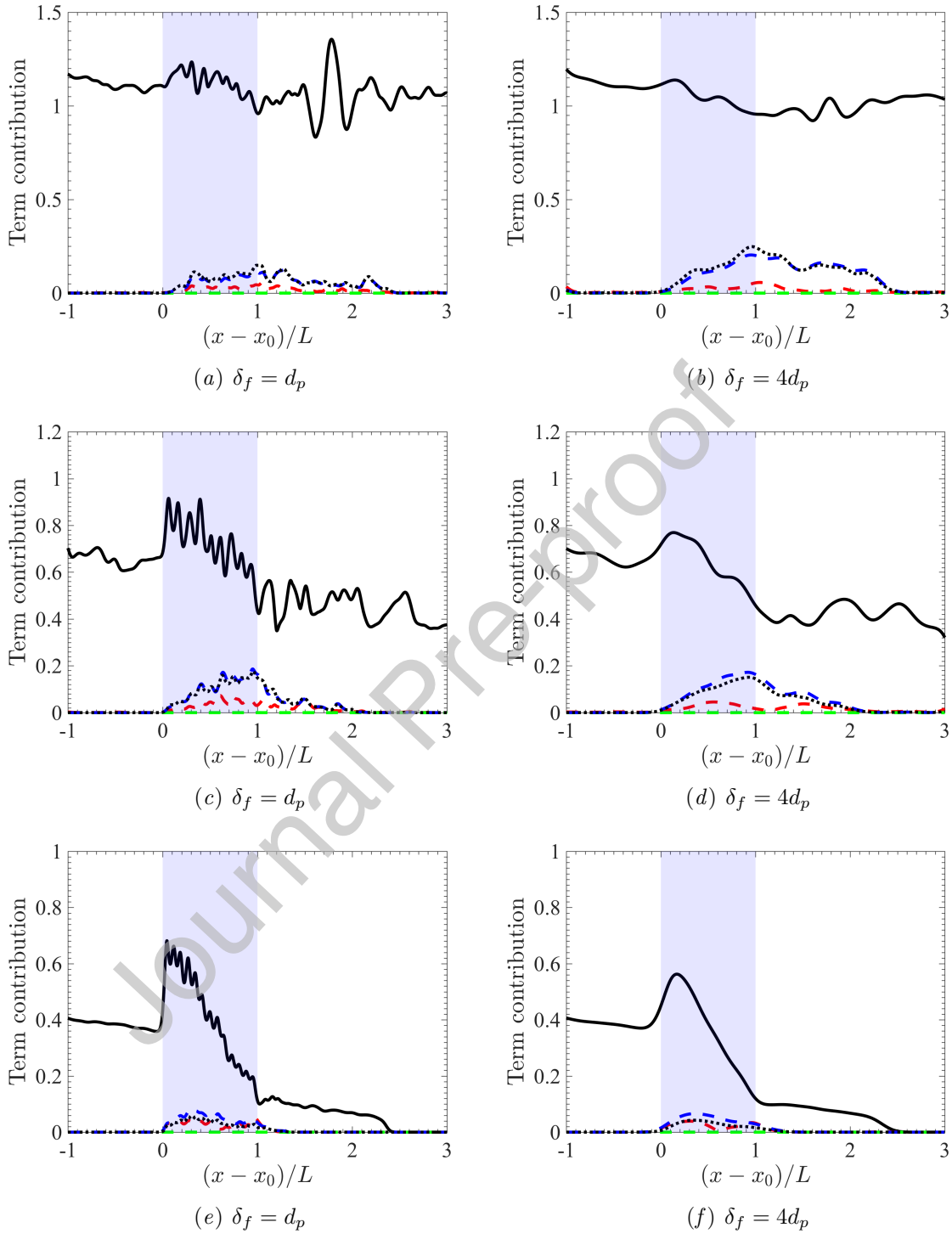

Figure 7: Magnitude of the Favre averaged sub-filtered stresses appearing in Eq. (30) as a function of filter size for $(a) - (b)$ $\varphi_p = 0.04$, $(c) - (d)$ $\varphi_p = 0.21$, and $(e) - (f)$ $\varphi_p = 0.44$ when $t = 2.334$. $\langle|\overline{p}\widetilde{\boldsymbol{u}}|\rangle_y$ (—), $\langle|\boldsymbol{R}_{Tu}|\rangle_y$ (- - -), $\langle|\boldsymbol{R}_{\tau u}|\rangle_y$ (- - -), $1/2\langle|\boldsymbol{R}_{uu}|\rangle_y$ (·····), and $\langle|\boldsymbol{R}_u \cdot \widetilde{\boldsymbol{u}}|\rangle_y$ (- - -) normalized by $\rho_1 u_1^3$. The shaded region (■) indicates particle location.

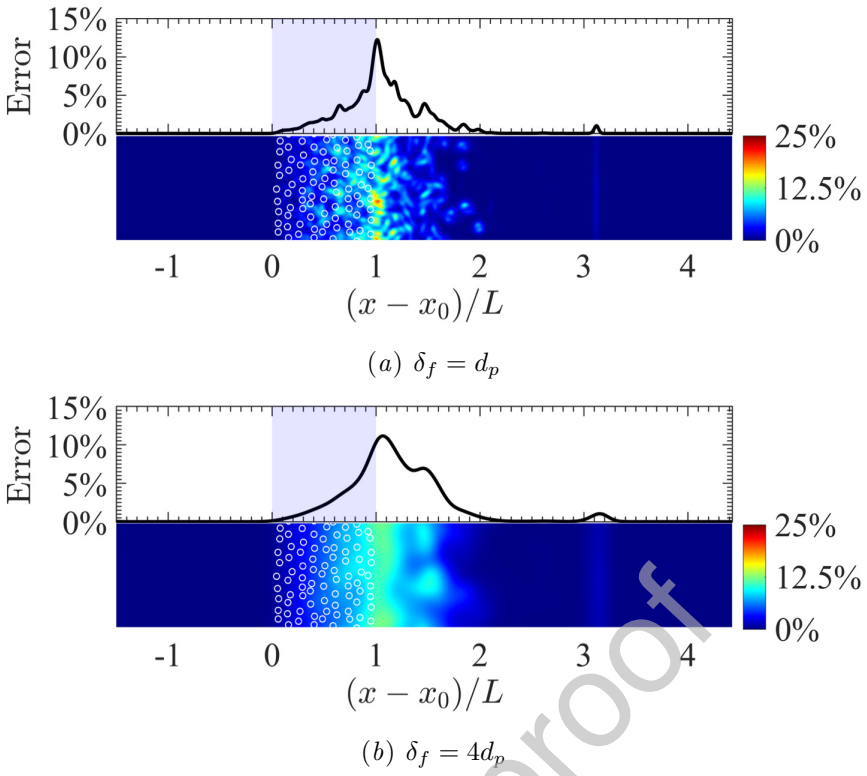

Figure 8: Error in the pressure field as a consequence of excluding PTKE in Eq. 33 for $\varphi_p = 0.21$ when $t = 2.334$. Averaged error (—) and local error (color). The shaded region (▮) indicates particle location.

wake structures in regions void of particles. To this end, a transport equation for the PTKE was derived in Sec. 2.3.5 using a consistent set of volume filtering operators.

Starting from Eq. (34), replacing $\boldsymbol{R}_{uu} = 2\boldsymbol{u} \cdot \boldsymbol{R}_u$ (as justified in Sec. 3.5), and rearranging and consolidating terms yields

$$\frac{\partial \alpha\rho k}{\partial t} + \nabla \cdot (\alpha\rho \boldsymbol{u} k) + \alpha \boldsymbol{R}_u : \nabla \boldsymbol{u} = (\boldsymbol{u}_p - \boldsymbol{u}) \cdot \boldsymbol{\mathcal{F}} - \alpha\rho\varepsilon_{PT}, \tag{36}$$

where the viscous and sub-filtered contributions have been absorbed into ε_{PT}, which represents dissipation of PTKE. Note that the terms involving resolved pressure and viscous stresses appearing on the second line of Eq. (34) contribute to the generation of internal energy and thus are not included in Eq. (36).

Following what is typically done in turbulence modeling [64], the dissipation rate is modeled as $\varepsilon_{PT} \propto k/\tau_\varepsilon$, where τ_ε is a dissipation time scale that requires modeling. A common approach is to assume the sub-filtered velocity fluctuations are dissipated on a time scale $\tau_1 = \mathcal{L}/\sqrt{k}$, with $\mathcal{L}$ an integral length scale that is anticipated to be on the order of d_p. Another candidate time scale for multiphase flows is $\tau_2 = \mathcal{L}/|\boldsymbol{u}_f - \boldsymbol{u}_p|$. In the present study, it was found that both definitions predict similar distributions of PTKE but τ_2 yields better magnitudes. However, the slip velocity is ill-defined in regions void of particles. To this end, we propose to blend the two time scales according to

$$\varepsilon_{PT} = f_\alpha \frac{C_f k}{\tau_1} + (1 - f_\alpha) \frac{C_f k}{\tau_2}, \tag{37}$$

where C_f is a constant that requires closure and f_α is a blending function. The function f_α takes the following form to ensure the time scale based on the slip velocity is only

used in the presence of particles

$$f_\alpha = \tanh\left(\frac{50}{\max(\alpha_p)}\alpha_p\right). \tag{38}$$

Based on the work of Mehrabadi et al. [33], the pseudo-turbulent Reynolds stress tensor is reconstructed from the PTKE according to

$$\boldsymbol{R}'_u = 2\rho k\left(\boldsymbol{b} + \frac{1}{3}\mathbb{I}\right), \tag{39}$$

where $\boldsymbol{R}'_u$ is the Reynolds stress aligned with the local slip velocity and $\boldsymbol{b}$ is the anisotropic stress tensor defined as

$$\boldsymbol{b} = f_\alpha \begin{bmatrix} b_{||} & 0 & 0 \\ 0 & b_\perp & 0 \\ 0 & 0 & b_\perp \end{bmatrix}. \tag{40}$$

The component parallel to the slip velocity is given by

$$b_{||} = \frac{a}{1 + b\exp(-c\mathrm{Re}_p)}\exp\left(\frac{d\ \alpha_p}{1 + e\exp(-f\mathrm{Re}_p)}\right), \tag{41}$$

and $b_\perp = -b_{||}/2$ is the perpendicular component such that $\mathrm{tr}(\boldsymbol{b}) = 0$. The pseudo-turbulent Reynolds stress tensor must be rotated to align with the Cartesian coordinate system. Details on the implementation of the rotation matrix can be found in [43]. For homogeneous, statistically stationary, incompressible gas-solid flows, the model constants are [33] $a = 0.523$, $b = 0.305$, $c = 0.114$, $d = 3.511$, $e = 1.801$, and $f = 0.005$. In Eq. (41), Re_p is the particle Reynolds number, which is first computed at the location of each particle then projected to the Eulerian grid. The Reynolds number at the i-th particle is defined as $\mathrm{Re}_p^{(i)} = \alpha\rho|\boldsymbol{u} - \boldsymbol{v}_p^{(i)}|d_p/\mu$. Details on the projection method are provided in Sec. 4.2.3.

It is important to note that the model for the anisotropic stress tensor was originally developed for Eulerian–Eulerian methods. A correction needs to be applied to handle anisotropy in regions void of particles where Re_p is undefined. One choice is to set $\mathrm{Re}_p = 0$ away from particles. However, by inspection of Eq. (41), in the limit of zero Reynolds number, the parallel component of the aligned tensor approaches $b_{||} \to a/(1+b)$. In this work, the anisotropic stress tensor is multiplied by f_α such that it smoothly approaches zero away from particles. Thus when $\alpha_p \to 0$, $\boldsymbol{b} = 0$ and the pseudo-turbulent Reynolds stress becomes isotropic.

In summary, a transport equation is introduced for the PTKE, and an algebraic model is employed to reconstruct $\boldsymbol{R}_u$. As a consequence, anisotropy is only predicted in the vicinity of particles, though finite PTKE can exist away from particles. Drag acts to produce PTKE in regions of finite slip velocity according to $(\boldsymbol{u}_p - \boldsymbol{u})\cdot\boldsymbol{\mathcal{F}}$, and ε_{PT} dictates its magnitude. A key aspect of the proposed PTKE modeling approach is that it is agnostic to the drag model employed. A natural choice is to use the drag correlation proposed by Tenneti et al. [57] to close $\boldsymbol{\mathcal{F}}$, since it is based on the the same DNS data used to develop the anisotropic stress model in [33]. However, the drag model of Tenneti et al. [57] is only valid when $\mathrm{Re}_p \lessapprox 300$. For the shock particle interactions considered here, Re_p is found to exceed 1000. In our previous work [49], we showed that the drag correlation of Gidaspow [19] yields the best results during shock-particle interactions of moderately dense systems due to the volume fraction and high Reynolds number corrections. While

Conservation of mass

$$\frac{\partial \alpha\rho}{\partial t} + \nabla \cdot (\alpha\rho\boldsymbol{u}) = 0$$

Conservation of momentum

$$\frac{\partial \alpha\rho\boldsymbol{u}}{\partial t} + \nabla \cdot (\alpha \{\rho\boldsymbol{u} \otimes \boldsymbol{u} + \boldsymbol{R}_u\}) = \alpha\nabla \cdot (\boldsymbol{\tau} - p\mathbb{I}) + \boldsymbol{\mathcal{F}}$$

Conservation of energy

$$\begin{aligned}\frac{\partial \alpha\rho E}{\partial t} &+ \nabla \cdot (\alpha\boldsymbol{u} \{\rho E + p\} + \alpha\boldsymbol{u} \cdot \{\boldsymbol{R}_u - \boldsymbol{\tau}\}) \\ &= -\alpha\nabla \cdot \boldsymbol{q} - (p\mathbb{I} - \boldsymbol{\tau}) : \nabla (\alpha_p \boldsymbol{u}_p) + \boldsymbol{u}_p \cdot \boldsymbol{\mathcal{F}} + \mathcal{Q}\end{aligned}$$

Pseudo-turbulent kinetic energy

$$\frac{\partial \alpha\rho k}{\partial t} + \nabla \cdot (\alpha\rho\boldsymbol{u}k) + \alpha\boldsymbol{R}_u : \nabla\boldsymbol{u} = (\boldsymbol{u}_p - \boldsymbol{u}) \cdot \boldsymbol{\mathcal{F}} - \alpha\rho\varepsilon_{PT}$$

Table 1: A summary of gas-phase volume filtered equations of motion.

new Mach number-dependent drag laws valid in high volume fraction regimes are needed, the drag model proposed by Gidaspow [19] is adopted in the present study. Details on the drag implementation will be provided in Sec. 4.2.2.

4.2. Discretization of the volume-filtered equations

4.2.1. Gas-phase description

The volume-filtered equations of motion summarized in Table 1 are discretized using the same high-order, energy-stable methods presented in Sec. 3.2. To avoid spurious oscillations near particles that may arise even when the flow field is at rest, the volume fraction must be removed from the conserved variables prior to adding dissipation, i.e., the SBP dissipation is based on high-order derivatives of $\vec{Q}/\alpha$. Here, $\vec{Q} = [\alpha\rho,\ \alpha\rho\boldsymbol{u},\ \alpha\rho E]^\mathsf{T}$ is the vector of conserved gas-phase variables.

4.2.2. Particle-phase description

While the proposed volume-filtered equations can be implemented in an Eulerian–Eulerian or Eulerian–Lagrangian framework, the present work considers the latter. Volume filtering the fluid stresses at the particle surface results in resolved and unresolved contributions to the interphase exchange term [8]. With this, the velocity of the i-th particle can be expressed as

$$m_p \frac{\mathrm{d}\boldsymbol{v}_p^{(i)}}{\mathrm{d}t} = \mathcal{V}_p \nabla \cdot (-p\mathbb{I} + \boldsymbol{\tau}) + \boldsymbol{f}_{\text{drag}}^{(i)}, \tag{42}$$

where $m_p = \pi\rho_p d_p^3/6$ is the particle mass and the unresolved portion, $\boldsymbol{f}_{\text{drag}}^{(i)}$, is typically modeled using a drag correlation. Other unresolved gas-particle interactions (e.g., Basset,

lift, etc.) would appear here. In this work, $\boldsymbol{f}^{(i)}_{\text{drag}}$ is given by

$$\frac{\boldsymbol{f}^{(i)}_{\text{drag}}}{m_p} = \frac{3}{4}\frac{\rho}{\rho_p} C_D \frac{\alpha|\boldsymbol{u} - \boldsymbol{v}^{(i)}_p|}{d_p}\left(\boldsymbol{u} - \boldsymbol{v}^{(i)}_p\right) \tag{43}$$

where C_D the coefficient of drag. Here, the particle equations are non-dimensionalized using the same reference quantities used in Eqs. (1)–(6).

The evolution of particle temperature is given by

$$m_p C_{p,p} \frac{\mathrm{d}T^{(i)}_p}{\mathrm{d}t} = \mathcal{V}_p \nabla \cdot \boldsymbol{q} + \boldsymbol{q}^{(i)}_{\text{inter}}, \tag{44}$$

where $T^{(i)}_p$ is the temperature of the i-th particle and $C_{p,p}$ is the ratio of particle-to-fluid heat capacity. The sub-filtered heat flux, $\boldsymbol{q}^{(i)}_{\text{inter}}$, is given by

$$\frac{\boldsymbol{q}^{(i)}_{\text{inter}}}{m_p} = \frac{\mathrm{Nu}}{3\tau_p \mathrm{Pr}}(T - T^{(i)}_p), \tag{45}$$

where Nu is the Nusselt number modeled using the correlation of Gunn [20].

4.2.3. Consistent interphase exchange

In order to compute the interphase exchange terms appearing in the gas-phase equations (α, $\boldsymbol{u}_p$, $\boldsymbol{\mathcal{F}}$, and $\mathcal{Q}$) consistent with the volume filtered formulation, the particle data is projected to the mesh using a filter kernel, $\mathcal{G}$, of size δ_f. The interphase exchange terms are given by

$$\alpha = 1 - \sum_{i=1}^{N_p} \mathcal{G}\left(|\boldsymbol{x} - \boldsymbol{x}^{(i)}_p|\right) \mathcal{V}_p, \tag{46}$$

$$\boldsymbol{\mathcal{F}} = -\sum_{i=1}^{N_p} \mathcal{G}\left(|\boldsymbol{x} - \boldsymbol{x}^{(i)}_p|\right) \boldsymbol{f}^{(i)}_{\text{drag}}, \tag{47}$$

$$\boldsymbol{u}_p \cdot \boldsymbol{\mathcal{F}} = -\sum_{i=1}^{N_p} \mathcal{G}\left(|\boldsymbol{x} - \boldsymbol{x}^{(i)}_p|\right) \boldsymbol{v}^{(i)}_p \cdot \boldsymbol{f}^{(i)}_{\text{drag}}, \tag{48}$$

and

$$\mathcal{Q} = -\sum_{i=1}^{N_p} \mathcal{G}\left(|\boldsymbol{x} - \boldsymbol{x}^{(i)}_p|\right) \boldsymbol{q}^{(i)}_{\text{inter}}. \tag{49}$$

The numerical implementation of Eqs. (46)–(49) requires special care. Maxey et al. [32] proposed to distribute the interphase coupling terms within a narrow envelope centered on the particle position to provide a local spatial average (or filtering) of the particle data on the mesh. However, a direct solution to this interphase coupling strategy is in general computationally intensive as it requires each particle to loop through a large number of neighboring grid points. More recently, Pepiot and Desjardins [44] proposed to project the particle data to the mesh using a high-order quintic spline kernel with compact support. To avoid excessive cost, the support of the kernel was set to the local grid spacing. However, such an approach will fail to converge under mesh refinement since the kernel support is proportional to the grid spacing. To address these shortcomings, Capecelatro and Desjardins [8] proposed a two step filtering approach that decouples

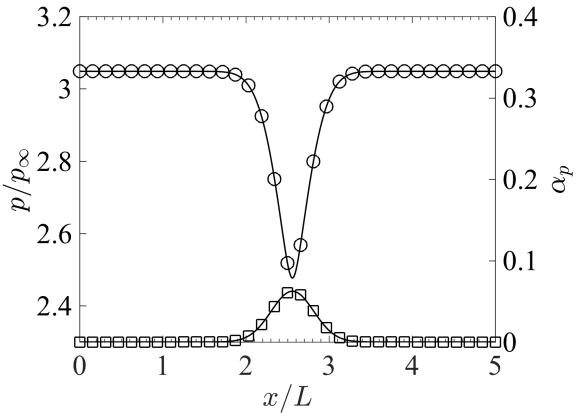

(a) Numerical solution of the gas-phase pressure at steady state normalized by the ambient pressure p_∞ (○) with a prescribed volume fraction (□). Analytic solutions (—).

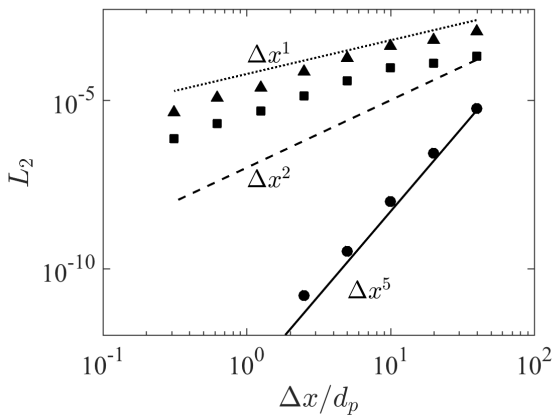

(b) L_2 error of the pressure profile at steady state during grid refinement using a filter size of $\delta_f = 0.1L$ (▲), $\delta_f = 0.2L$ (■), and a prescribed volume fraction field (●).

Figure 9: Verification of a converging-diverging nozzle.

the mesh size from particle diameter ratio in an efficient manner. First, particle data is sent to neighboring grid points via trilinear extrapolation. The solution is then diffused such that the projection resembles a Gaussian with characteristic size of δ_f. To avoid restrictive time step constraints in the diffusion process, the latter step is solved implicitly via approximate factorization with a second order alternating direction implicit (ADI) scheme.

4.3. Verification – a converging-diverging nozzle

Verification of the VF-EL framework is conducted in the context of a one-dimensional converging-diverging nozzle. In this example, the area change is a consequence of the local change in volume fraction. Particles are placed within a length L with varying spacing such that the area change due to the corresponding volume fraction distribution is approximately Gaussian. The volume fraction distribution is centered in a domain of size $L_x = 5.12L$. The gas-phase density, velocity, and pressure are initialized with post-shock conditions for a shock Mach number of $\mathrm{Ma}_s = 1.66$, given by $(\rho,\ u,\ p) = (2.131,\ 0.881,\ 2.177)$. An analytic solution for the resulting pressure profile can be found in Liepmann and Roshko [27].

Two methods are employed to define the volume fraction field. First, the volume fraction is prescribed analytically as a smoothly varying Gaussian function with a standard deviation of $L/4$ and maximum value of 0.08. (see Fig. 9(a)). These parameters were chosen such that the minimum nozzle area is below the critical area for a choked flow. In the second approach, Lagrangian particles are used to generate the volume fraction field according to Eq. (46) to test the convergence of the two-way coupling scheme. In this approach, particles with diameters $d_p = 1.0 \times 10^{-3}L$ are spaced such that the volume fraction distribution resembles the Gaussian distribution employed in the first approach. Two interphase filter sizes are considered for this example, $\delta_f = 0.1L$ and $\delta_f = 0.2L$.

A grid refinement study is performed by varying the grid spacing $0.3 \leq \Delta x/d_p \leq 40$ and the simulations are run until they reach steady state. As shown in Fig. 9(b), convergence of the steady-state pressure field towards the analytic solution is achieved in both

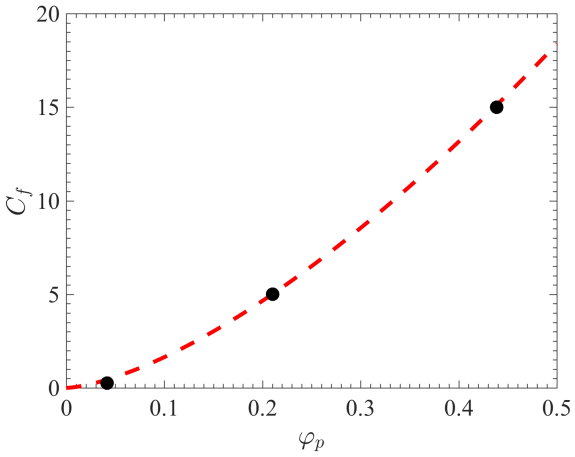

Figure 10: Power-law fit of the coefficient appearing in the dissipation model (37) to the two-dimensional simulations. Values extracted from DNS (•) and $C_f = 52\varphi_p^{1.5}$ (- - -).

approaches. When the volume fraction is prescribed, the L_2 error norm converges with 5-th order accuracy, consistent with the SBP-SAT discretization described in Sec. 3.2. Although lower convergence is observed when the volume fraction is generated from the two-way coupling scheme, the two-step filter ensures the solution converges to the analytic result even when $\Delta x < d_p$. The reduction in convergence when Lagrangian particles are considered is a consequence of the ADI scheme used in the implicit filtering operation. The convergence rate also depends on the smoothness of the volume fraction field, as seen when the value of δ_f is varied. Employing higher-order filters or mollification kernels can be used to improve the convergence rate, albeit at a higher cost.

4.4. Modeling PTKE in a two-dimensional shock-particle configuration

In this section, VF-EL simulations are compared against the two-dimensional particle-resolved simulations reported in Sec. 3. A shock with a Mach number $\mathrm{Ma}_s = 1.66$ interacts with stationary particles using the same particle distribution employed in the DNS. The ratio of particle-to-fluid heat capacity is $C_{p,p} = 0.8375$, corresponding to soda-lime particles in air. The integral length scale appearing in the dissipation model (37) is taken to be $\mathcal{L} = d_p$. A domain is discretized using a uniform grid of size 263×36–approximately 20 times smaller in each direction compared to the DNS–such that there are approximately two points across the diameter of each Lagrangian particle. The filter size is taken to be $\delta_f = 4d_p$, however, the results reported here remain relatively unchanged for $2 \leq \delta_f/d_p \leq 8$. Finally, we note that the coefficients used in the anisotropy model (39)–(41) were derived for three-dimensional flows. Using this model in two dimensions yields negative normal components of the Reynolds stress tensor. Thus, in this section, $\boldsymbol{R}_u$ is taken to be isotropic. The efficacy of the anisotropic model will be assessed in the following section.

A key parameter appearing in the coupled set of volume filtered equations (summarized in Table 1) is C_f from the PTKE dissipation model (37). It was found that $C_f = 0.25,\ 5.0,$ and 15.0 yields the best agreement in PTKE for $\varphi_p = 0.04,\ 0.21,$ and 0.44, respectively. This dependence on volume fraction is expected, since wakes interact more strongly with each other and the particles as φ_p increases. Based on these results,

Ma_s	Shock Mach number	1.22	1.66	3.00
ρ_1	Post-shock density	1.376	2.131	3.857
p_1	Post-shock pressure	1.121	2.177	7.381
u_1	Post-shock velocity	0.334	0.881	2.222
φ_p	Mean volume fraction	0.10	0.19	
N_p	Number of particles	200	400	
	Grid Resolution	DNS [35]	VF-EL	
		$\sim 16 - 18 \times 10^6$	$131 \times 10 \times 10$	
		tetrahedral cells		

Table 2: Parameters used in the three-dimensional shock-particle simulations. All simulations are performed with pre-shock conditions of $\rho_2 = 1$, $p_2 = 0.714$, and $u_2 = 0$. VF-EL is performed with $\delta_f = 4d_p$ and $\Delta x = d_p$. Further details on the DNS can be found in Mehta et al. [35, 36, 37, 38].

a power-law fit was obtained for C_f (see Fig. 10) according to

$$C_f \approx 52\varphi_p^{1.5}. \tag{50}$$

This dependency will change in three dimensions, and also depend on the shock Mach number and drag model employed (see Sec. 4.5). We note that coarser grid resolutions and larger filter sizes were found to have negligible effects on the values of C_f.

Overall good agreement can be observed in the prediction of PTKE between the model and DNS (see Fig. 11). For a fixed value of C_f, VF-EL captures the magnitude and distribution of PTKE over the time horizon considered. It should be noted that the bi-modal behavior observed in the DNS at early times is a result of the transmitted and reflected shocks. Because this sub-filtered contribution is purely hydrodynamics, i.e., it would appear even in the absence of particles, it should not be expected to be captured by the PTKE model. It is notable that the model is capable of predicting PTKE within the particle curtain as well as downstream in regions void of particles.

A comparison between the spatial distribution of PTKE is shown in Fig. 12 corresponding to the conditions reported in Fig. 11(e). Despite a factor of approximately 400 reduction in grid resolution, VF-EL captures the main features of the spatial distribution exceptionally well. Any discrepancy seen between DNS data and VF-EL can be attributed to the unresolved contributions of sub-filtered terms, which were lumped into ε_{PT}, and by neglecting anisotropy.

As mentioned in Sec 3.5, neglecting the effect of PTKE will systematically act to over-predict the local pressure and as a consequence may result in errors in the local Mach number. As shown in Fig. 13, the instantaneous fields reveal under-predictions in Mach number when VF-EL is performed without the PTKE model. The maximum local Mach number is located near the downstream edge of the particles with a value of approximately $\mathrm{Ma} = 0.63$ when PTKE is accounted for and $\mathrm{Ma} = 0.61$ when PTKE is neglected. While the magnitudes are relatively close, the distribution of Mach number differs, namely at the downstream edge of the particles where choking followed by supersonic expansion was observed in the DNS.

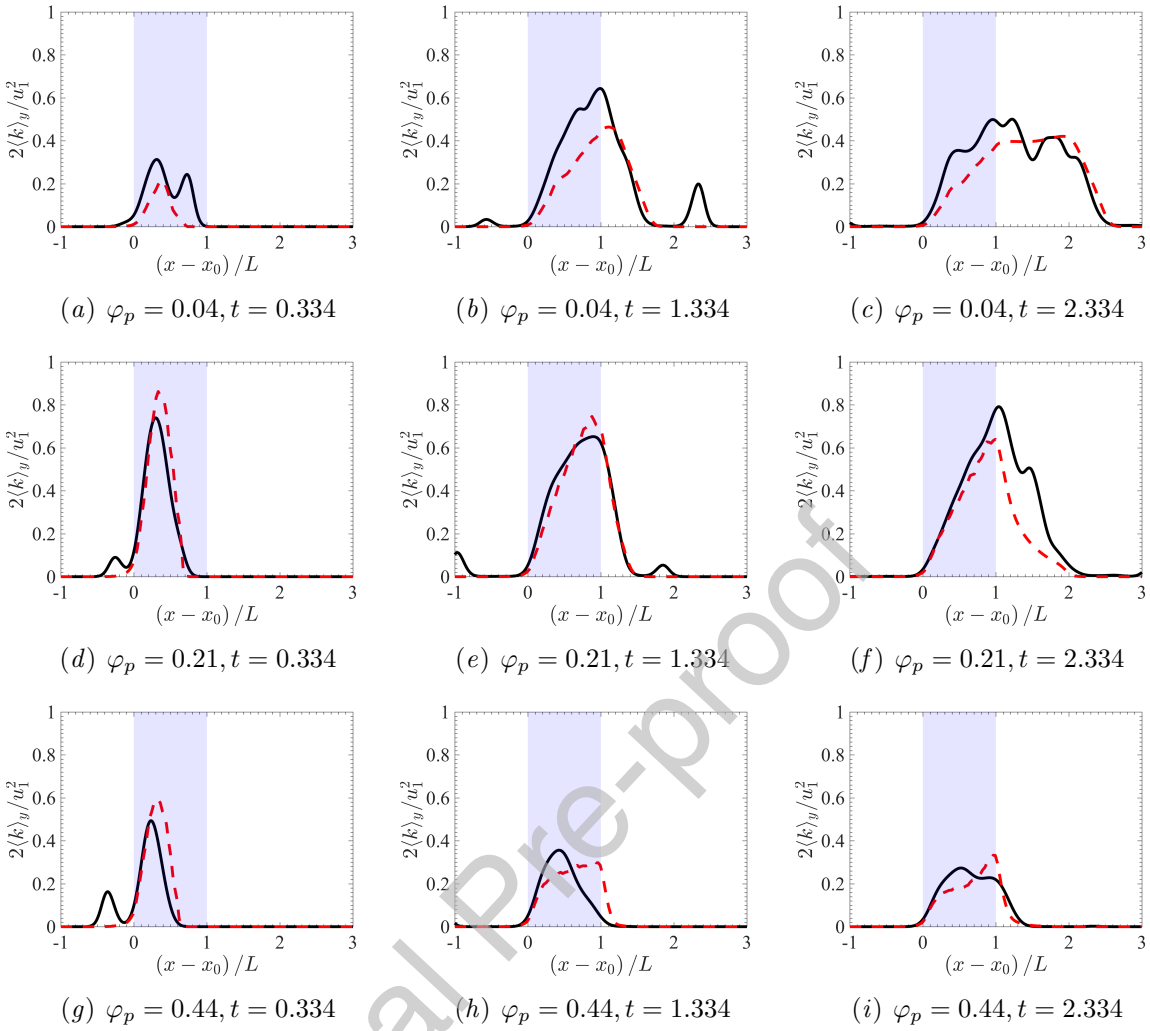

Figure 11: Comparison of PTKE from filtered DNS (—) and VF-EL (- - -) with $\delta_f = 4d_p$. Coefficients of $C_f = 0.25,\ 5.0,$ and 15.0 were used for $\varphi_p = 0.04,\ 0.21,$ and 0.44, respectively. The shaded region (▒) indicates particle location.

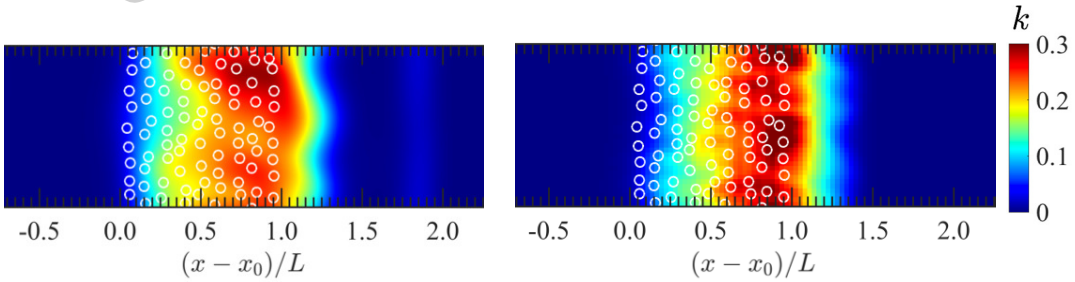

Figure 12: Instantaneous snapshot of PTKE from the two-dimensional VF-EL with $\varphi_p = 0.21$ at $t = 1.334$.

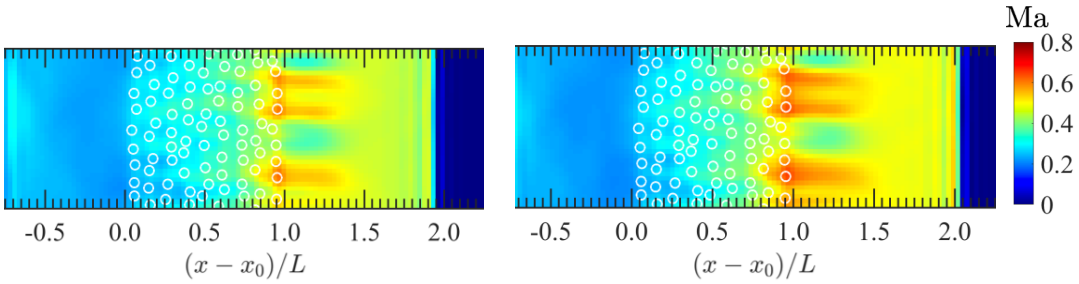

(a) VF-EL without PTKE (b) VF-EL with PTKE

Figure 13: Instantaneous snapshot of local Mach number from the two-dimensional VF-EL with $\varphi_p = 0.21$ at $t = 1.334$.

4.5. Modeling PTKE in a three-dimensional shock-particle configuration

In this section, the results obtained from VF-EL are compared against the three-dimensional particle-resolved simulations of Mehta et al. [35]. Simulations are performed for three shock Mach numbers: $\mathrm{Ma}_s = 1.22$, 1.66, and 3.00, and two mean particle volume fractions: $\varphi_p = 0.10$ and 0.19. Particles of size $d_p^\star = 100$ µm are randomly distributed over a length of $L^* = 1.7$ mm in a shock tube with a cross section of $L_y^\star \times L_z^\star = 0.8\,\mathrm{mm} \times 0.8\,\mathrm{mm}$. Particles are taken to be stationary with the same material properties described in the previous section. A uniform grid is employed in VF-EL such that $\Delta x = d_p$ with $\delta_f = 4d_p$. The integral length scale appearing in the dissipation model (37) is taken to be $\mathcal{L} = d_p$. A summary of the simulation parameters can be found in Table 2. It should be noted that the plots are normalized by post-shock conditions, which vary for different shock Mach numbers. Due to the availability of DNS data, comparisons are only performed at early times prior the transmitted shock passing through the particle suspension.

In order to accurately predict the distribution of pseudo-turbulent Reynolds stresses, appropriate values of C_f must be chosen. The values of C_f are determined by finding the best fit for $\rho k = \mathrm{tr}(\boldsymbol{R}_u)/2$ (see Fig. 14). Even with $\mathcal{O}(10^3)$ reduction in resolution compared to the DNS, the PTKE predicted by VF-EL exhibits overall excellent agreement with the DNS for the range of shock Mach numbers and volume fractions under consideration. Perhaps surprisingly, the largest discrepancies are observed in the lowest Mach number case. In addition, the algebraic model used to reconstruct the separate components of the pseudo-turbulent Reynolds stress is able to predict the level of anisotropy reasonably well, despite it being developed for incompressible flows (see Fig. 15). In general, the Reynolds stresses increase with increasing volume fraction and shock Mach number.

As was seen in the two-dimensional simulations, C_f increases with increasing volume fraction. The magnitude of the Reynolds stresses were found to be smaller in three dimensions, consistent with previous work [35], and consequently the magnitude of C_f is larger. Here, it was found that C_f increases with decreasing shock Mach number according to $C_f = 150\mathrm{Ma}_s^{-10} + 83\varphi_p - 2$. (see Fig. 16). This could indicate that contributions that are lumped into the dissipation model are more significant at lower shock Mach numbers relative to the drag production term.

As noted earlier, the drag correlation of Gidaspow [19] was used due to its applicability at high Reynolds numbers and volume fractions. The effect of different drag correlations on the pseudo-Reynolds stresses are reported in Appendix C. It is found that the modeling coefficient, C_f, changes with drag law; however, the distribution of Reynolds

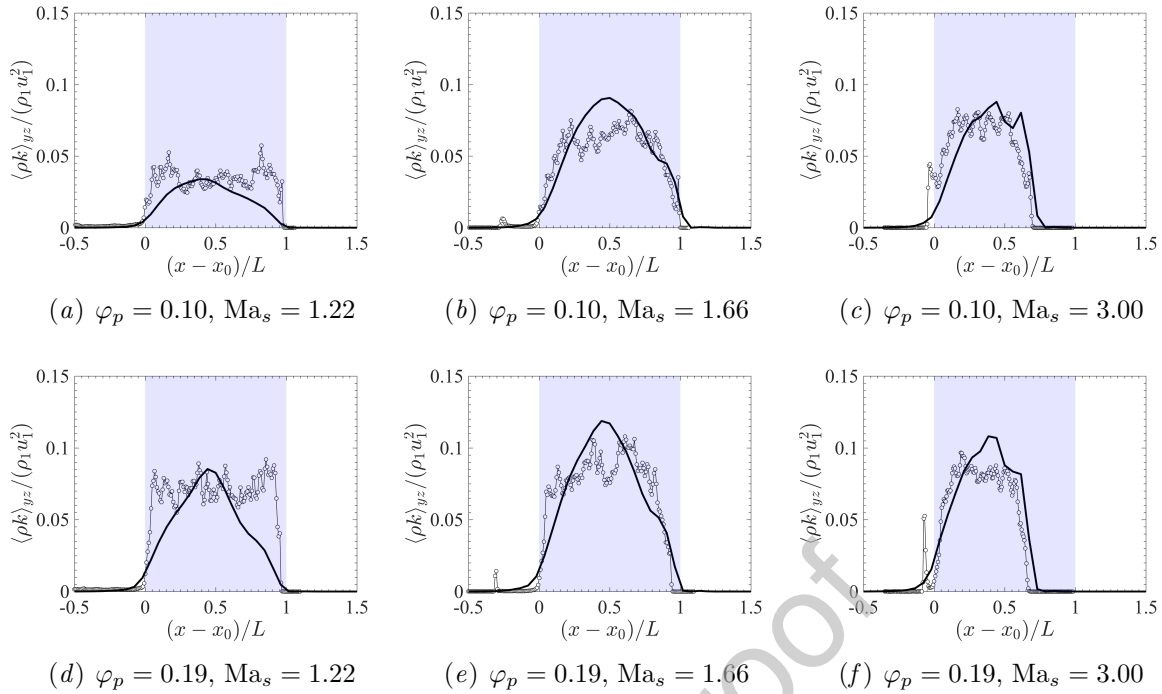

(a) $\varphi_p = 0.10$, $\mathrm{Ma}_s = 1.22$ (b) $\varphi_p = 0.10$, $\mathrm{Ma}_s = 1.66$ (c) $\varphi_p = 0.10$, $\mathrm{Ma}_s = 3.00$

(d) $\varphi_p = 0.19$, $\mathrm{Ma}_s = 1.22$ (e) $\varphi_p = 0.19$, $\mathrm{Ma}_s = 1.66$ (f) $\varphi_p = 0.19$, $\mathrm{Ma}_s = 3.00$

Figure 14: Averaged $\rho k = \mathrm{tr}(\boldsymbol{R}_u)/2$ obtained from DNS [35] (-O-) and VF-EL (—) as a function of Mach number and volume fraction. $\mathrm{Ma}_s = 1.22$ evaluated at $t = 0.818$, $\mathrm{Ma}_s = 1.66$ at $t = 0.620$, and $\mathrm{Ma}_s = 3.00$ at $t = 0.237$. The shaded region ( ) indicates particle location.

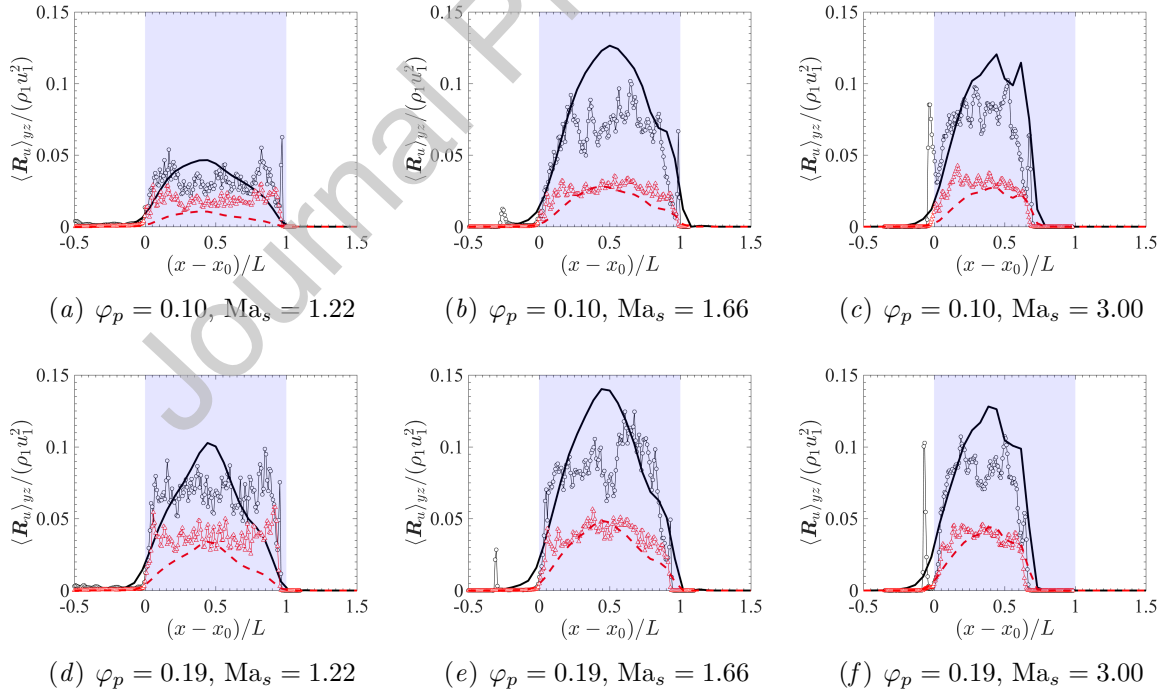

(a) $\varphi_p = 0.10$, $\mathrm{Ma}_s = 1.22$ (b) $\varphi_p = 0.10$, $\mathrm{Ma}_s = 1.66$ (c) $\varphi_p = 0.10$, $\mathrm{Ma}_s = 3.00$

(d) $\varphi_p = 0.19$, $\mathrm{Ma}_s = 1.22$ (e) $\varphi_p = 0.19$, $\mathrm{Ma}_s = 1.66$ (f) $\varphi_p = 0.19$, $\mathrm{Ma}_s = 3.00$

Figure 15: Components of the pseudo-turbulent Reynolds stress obtained from DNS [35] (symbols) and VF-EL (lines) as a function of Mach number and volume fraction. $\mathrm{Ma}_s = 1.22$ evaluated at $t = 0.818$, $\mathrm{Ma}_s = 1.66$ at $t = 0.620$, and $\mathrm{Ma}_s = 3.00$ at $t = 0.237$. DNS $R_u(1,1)$ (-O-), DNS $(R_u(2,2) + R_u(3,3))/2$ (-△-), VF-EL $R_u(1,1)$ (—), and VF-EL $(R_u(2,2) + R_u(3,3))/2$ (- - -). The shaded region ( ) indicates particle location.

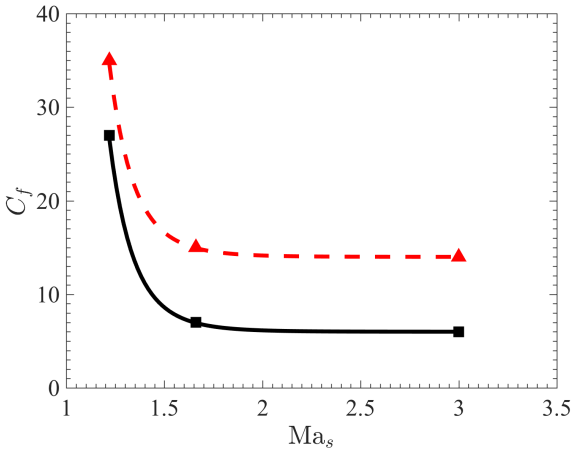

Figure 16: Coefficient appearing in the dissipation model (37) for three-dimensional simulations. Values extracted from $\varphi_p = 0.10$ (■) and $\varphi_p = 0.20$ (▲). Power-law fits for $\varphi_p = 0.10$ (—) and $\varphi_p = 0.19$ (- - -) given by $C_f = 150\mathrm{Ma}_s^{-10} + 83\varphi_p - 2$.

stresses remain unchanged. Further analysis is required to model C_f over a wider range of conditions. For example, based on the work of Osnes et al. [39], C_f will also likely depend on d_p. In conclusion, given an adequate model for C_f, the transport equation proposed here is capable of accurately predicting the distribution of PTKE (irrespective of the drag law employed). In the present work, C_f was fit to particle-resolved simulations of stationary particles, and is thus limited to applications of fixed particles under the volume fractions and Mach numbers considered here. Future work is needed to extend this approach to include a physics-based model for dissipation.

5. Conclusions

In this work, we extend the volume-filtered formulation of Anderson and Jackson [1] to compressible two-phase flows. It was demonstrated that the energy equation requires special consideration. In particular, it is shown that alternative approaches can be taken during the derivation, resulting in different closure problems. A key outcome of the volume-filtered formulation is the appearance of the pseudo-turbulent kinetic energy (PTKE) in the state equation for pressure. It was shown that PTKE acts to systematically reduce the gas-phase pressure, and consequently increase the local Mach number.

Particle-resolved simulations of shock-particle interactions were performed to quantify the relative importance of unclosed terms via an *a posteriori* filtering approach consistent with the volume-filtered formulation. The relative importance of the unclosed terms appearing in the equations were shown to depend on the discretization employed, quantified by varying the filter size, δ_f. For sufficiently large filter sizes, ($\delta_f > 4d_p$), the majority of velocity fluctuations reside at the sub-filter scale. In general, PTKE was seen to depends on both δ_f and volume fraction. It was demonstrated that the PTKE dependence can be collapsed to a Knudsen number based on the mean inter-particle spacing.

A transport equation for the PTKE was then derived, which contains a production term proportional to the local drag force and slip velocity magnitude, and a dissipation rate that requires closure. Dissipation was modeled using an integral length scale proportional to the particle diameter in addition to a velocity scale that depends on the local slip

velocity when particles are present and the square of PTKE in regions void of particles. An algebraic model was employed to reconstruct the components of the pseudo-turbulent Reynolds stress.

The volume-filtered equations of motion were implemented within a high-order Eulerian–Lagrangian framework that admits convergence under grid refinement. A constant appearing in the dissipation rate was fit over a range of volume fractions and Mach numbers in both two-dimensional and three-dimensional shock-particle configurations. The Eulerian–Lagrangian approach was shown to be capable of predicting the distribution of pseudo-turbulent Reynolds stresses with the correct level of anisotropy.

In summary, the present study provides a framework to develop new models, beyond traditional ensemble averaging. While the present work focused on stationary particles, new models are needed to incorporate the effect of PTKE on particle dispersion. With the increasing availability of particle-resolved simulation data coming online (e.g., [35, 39, 61]), further improvements to the model can be made.

Acknowledgements

This work was supported by a NASA Space Technology Research Fellowship. Computational resources were provided by the Advanced Research Computing Technology Services at the University of Michigan. We would like to thank Dr. Mehta and Prof. Balachandar for sharing their pseudo-turbulent Reynolds stress data reported in Mehta et al. [35]. We also gratefully acknowledge Dr. David Buchta and Dr. Theo Theofanous for the impactful discussions throughout the preparation of this manuscript.

Appendix A. Methodology for *a posteriori* filtering

The method presented here is used for *a posteriori* filtering of DNS data in Sec. 3. An arbitrary quantity A computed using DNS on a mesh with resolution $\Delta x \ll d_p$ is separated into spatially filtered and residual contributions $A = \overline{A} + A'$ according to

$$\alpha\overline{A} = (\mathcal{I}A) \star \mathcal{G}, \tag{A.1}$$

where $\mathcal{I}$ is an indicator function that is 0 inside a particle and 1 in the fluid and $\mathcal{G}$ is a filter kernel. A direct solution to (A.1) is computationally expensive, and in general not tractable when working on large-scale DNS data. Consequently, the convolution integral is recast in Fourier space as

$$\widehat{\alpha\overline{A}} = \widehat{\mathcal{I}wA} \cdot \widehat{\mathcal{G}}, \tag{A.2}$$

where $\widehat{(\cdot)}$ indicates a quantity subject to a Fourier transform. Because the simulations performed in this study are not periodic in the x-direction, a windowing function, w, is applied to the quantity of interest prior to filtering. In this work, a Tukey window [62] is employed, defined as

$$w(i) = \begin{cases} \frac{1}{2}\left[1 + \cos\left(\frac{2\pi i}{r(N_x-1)} - \pi\right)\right] & 0 \le i < \frac{r(N_x-1)}{2} \\ 1 & \frac{r(N_x-1)}{2} \le i < (N_x-1)\left(1-\frac{r}{2}\right) \\ \frac{1}{2}\left[1 + \cos\left(\frac{2\pi i}{r(N_x-1)} - \frac{2\pi}{r} + \pi\right)\right] & (N_x-1)\left(1-\frac{r}{2}\right) < i \le (N_x-1) \end{cases}, \tag{A.3}$$

where $r = 0.05$ is the cosine tapering parameter, i is the grid point it is being applied to, and N_x is the total number of grid points in the x-direction. The cosine tapering

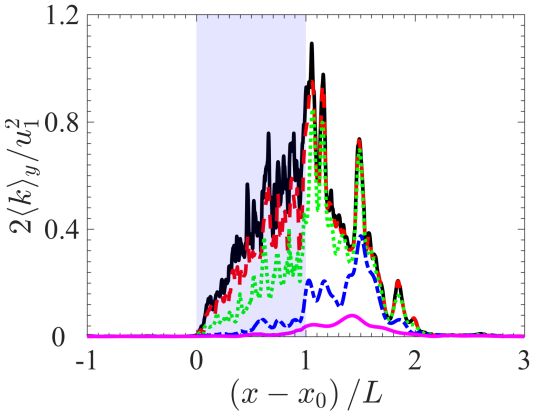

Figure B.17: Ensemble averaged PTKE obtained from DNS (—) and recovered from deconvolution with $\delta_f = d_p$ (- - -), $\delta_f = 2d_p$ (····), $\delta_f = 4d_p$ (-·-), and $\delta_f = 8d_p$ (—). Quantities are calculated for $\varphi_p = 0.21$ when $t = 2.334$. The shaded region ( ) indicates particle location.

parameter is selected such that that the windowing function does not interfere with the flow field, such as the transmitted and reflected shocks as well as the wake downstream of the particles.

Appendix B. Term reconstruction through approximate deconvolution

In this appendix we assess the accuracy of reconstructing the sub-filtered terms via a deconvolution procedure. While direct deconvolution is not possible due to the sparse nature of the filtering kernel, a common alternative is to use the approximate deconvolution method (ADM) [40, 46, 47, 50, 67]. This can be accomplished by convolving the approximate inverse of the filtering kernel

$$\hat{\mathcal{G}}^{-1} \approx \sum_{\nu=0}^{N} (1-\hat{\mathcal{G}})^{\nu} \tag{B.1}$$

with filtered quantities in Fourier space and then performing an inverse Fourier transform to get an approximation of the flow fields prior to filtering. Here, N is the desired truncation of the series expansion, set to $N = 100$ for this work, and $\hat{(\cdot)}$ denotes that the quantity is in Fourier space.

Reconstruction of ensemble averaged PTKE through deconvolution is shown in Fig. B.17. For a filter size of $\delta_f = d_p$, the deconvolution provides a good approximation of PTKE compared to ensemble averaging the DNS data. As the filter size increases, the PTKE calculated from deconvolution continues to decrease. As shown in Fig. 5, the unresolved PTKE should either increase or asymptote to some maximum unresolved quantity. While using ADM to approximate the unresolved quantities, it becomes more difficult to recover fluctuations for larger filter sizes and therefore unresolved stresses will be under predicted around the particle phase. While this method is limited to recovering stresses for smaller filter widths, it still has its utility. Other possible uses include the approximation of the unfiltered velocity to improve drag estimations and partial recovery of microscale flow fields during post-processing.

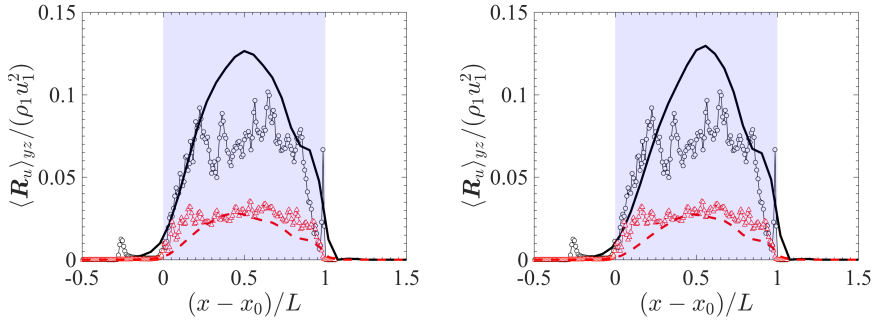

(*a*) Gidaspow [19], $C_f = 7$ (*b*) Schiller-Naumann [12], $C_f = 3$

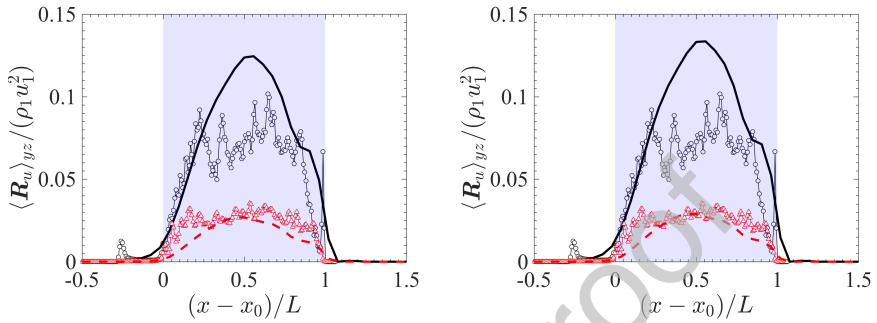

(*c*) Loth [30], $C_f = 5$ (*d*) Henderson [22], $C_f = 5$

Figure C.18: Effect of drag law on the components of the pseudo-turbulent Reynolds stress for $\varphi_p = 0.1$ and $\mathrm{Ma}_s = 1.66$ at $t = 0.62$. Same line types as in Fig. 15.

Appendix C. Drag dependence on PTKE

The PTKE model proposed in Sec. 4.1 is expressed for an arbitrary drag law. In this section, we extend the three-dimensional shock-particle analysis presented in Sec. 4.5 to evaluate the effect of drag laws on PTKE. Three additional drag laws are considered, each of which are valid under different flow conditions. We consider the Schiller-Naumann drag correlation [12] that depends on Reynolds number, the correlations proposed by Loth [30] and Henderson [22] that take into account Mach number effects, in addition to the drag correlation of Gidaspow [19] used throughout the present study that accounts for volume fraction effects and high Reynolds numbers.

As shown in Fig. C.18, the parameter C_f appearing in the dissipation rate are smaller for Schiller-Naumann, Loth, and Henderson compared to Gidaspow. This indicates that the relative drag production is lower under the same conditions. In this case, the lower drag will result in noticeably faster transmitted shocks and slower reflected shocks compared to the DNS. Regardless of the different behaviors in drag, the distributions of pseudo-turbulent Reynolds stresses are remarkably similar. The results suggest that similar trends in PTKE can be achieved for any of the drag laws used here, provided a reasonable value of C_f.

References

[1] Anderson, T.B., Jackson, R., 1967. Fluid mechanical description of fluidized beds. Equations of motion. Industrial & Engineering Chemistry Research 6, 527–539.

[2] Balachandar, S., Eaton, J., 2010. Turbulent dispersed multiphase flow. Annual Review of Fluid Mechanics 42, 111–133.

[3] Balachandar, S., Liu, K., Lakhote, M., 2019. Self-induced velocity correction for improved drag estimation in Euler–Lagrange point-particle simulations. Journal of Computational Physics 376, 160–185.

[4] Balakrishnan, K., Bellan, J., 2018. High-fidelity modeling and numerical simulation of cratering induced by the interaction of a supersonic jet with a granular bed of solid particles. International Journal of Multiphase Flow 99, 1–29.

[5] Beetham, S., Capecelatro, J., 2019. Biomass pyrolysis in fully-developed turbulent riser flow. Renewable energy 140, 751–760.

[6] Boukharfane, R., Ribeiro, F.H.E., Bouali, Z., Mura, A., 2018. A combined ghost-point-forcing/direct-forcing immersed boundary method (IBM) for compressible flow simulations. Computers & Fluids 162, 91–112.

[7] Buchta, D.A., Shallcross, G.S., Capecelatro, J., 2019. Sound and turbulence modulation by particles in high-speed shear flow. Journal of Fluid Mechanics In press, 578–635.

[8] Capecelatro, J., Desjardins, O., 2013a. An Euler–Lagrange strategy for simulating particle-laden flows. Journal of Computational Physics 238, 1–31.

[9] Capecelatro, J., Desjardins, O., 2013b. Eulerian-Lagrangian modeling of turbulent liquid-solid slurries in horizontal pipes. International Journal of Multiphase Flow 55, 64–79.

[10] Carpenter, M., Gottlieb, D., Abarbenel, S., 1994. Time-stable boundary conditions for finite difference schemes involving hyperbolic systems: methodology and application for high-order compact schemes. Journal of Computational Physics 111, 220–236.

[11] Chu, S., Prosperetti, A., 2016. On flux terms in volume averaging. International Journal of Multiphase Flow 80, 176–180.

[12] Clift, R., Grace, J., Weber, M., 1978. Bubbles, drops, and particles. Academic Press Incorporated.

[13] Davis, S.L., Jacobs, G.B., Sen, O., Udaykumar, H., 2017. SPARSE-A subgrid particle averaged Reynolds stress equivalent model: testing with a priori closure. Proceedings of the Royal Society A: Mathematical, Physical and Engineering Sciences 473, 20160769.

[14] DeMauro, E.P., Wagner, J.L., DeChant, L.J., Beresh, S.J., Turpin, A.M., 2019. Improved scaling laws for the shock-induced dispersal of a dense particle curtain. Journal of Fluid Mechanics 876, 881–895.

[15] Fox, R.O., 2012. Large-eddy-simulation tools for multiphase flows. Annual Review of Fluid Mechanics 44, 47–76.

[16] Freund, J.B., 1997. Proposed inflow/outflow boundary condition for direct computation of aerodynamic sound. AIAA Journal 35, 740.

[17] Gale, M., Buettner, K., Mehta, R., Liever, P.A., Curtis, J., 2017. Gas-granular flow solver for plume surface interaction and cratering simulations, in: 23rd AIAA Computational Fluid Dynamics Conference, p. 4503.

[18] Gibilaro, L.G., Gallucci, K., Di Felice, R., Pagliai, P., 2007. On the apparent viscosity of a fluidized bed. Chemical Engineering Science 62, 294–300.

[19] Gidaspow, D., 1994. Multiphase flow and fluidization: continuum and kinetic theory descriptions. Academic Press.

[20] Gunn, D.J., 1978. Transfer of heat and mass to particles in fixed and fluidised beds. International Journal of Heat and Mass Transfer 21, 467–476.

[21] Guo, L., Capecelatro, J., 2019. The role of clusters on heat transfer in sedimenting gas-solid flows. International Journal of Heat and Mass Transfer 132, 1217–1230.

[22] Henderson, C.B., 1976. Drag coefficients of spheres in continuum and rarefied flows. AIAA Journal 14, 707–708.

[23] Horwitz, J., Mani, A., 2016. Accurate calculation of stokes drag for point-particle tracking in two-way coupled flows. Journal of Computational Physics 318, 85–109.

[24] Hosseinzadeh-Nik, Z., Subramaniam, S., Regele, J.D., 2018. Investigation and quantification of flow unsteadiness in shock-particle cloud interaction. International Journal of Multiphase Flow 101, 186–201.

[25] Houim, R.W., Oran, E.S., 2016. A multiphase model for compressible granular–gaseous flows: formulation and initial tests. Journal of Fluid Mechanics 789, 166–220.

[26] Ireland, P.J., Desjardins, O., 2017. Improving particle drag predictions in Euler–Lagrange simulations with two-way coupling. Journal of Computational Physics 338, 405–430.

[27] Liepmann, H.W., Roshko, A., 2001. Elements of gasdynamics. Courier Corporation.

[28] Ling, Y., Balachandar, S., Parmar, M., 2016. Inter-phase heat transfer and energy coupling in turbulent dispersed multiphase flows. Physics of Fluids 28, 033304.

[29] Ling, Y., Wagner, J.L., Beresh, S.J., Kearney, S.P., Balachandar, S., 2012. Interaction of a planar shock wave with a dense particle curtain: Modeling and experiments. Physics of Fluids 24, 113301.

[30] Loth, E., 2008. Compressibility and rarefaction effects on drag of a spherical particle. AIAA Journal 46, 2219–2228.

[31] Mattsson, K., Svärd, M., Nordström, J., 2004. Stable and accurate artificial dissipation. Journal of Scientific Computing 21, 57–79.

[32] Maxey, M.R., Patel, B.K., Chang, E.J., Wang, L.P., 1997. Simulations of dispersed turbulent multiphase flow. Fluid Dynamics Research 20, 143.

[33] Mehrabadi, M., Tenneti, S., Garg, R., Subramaniam, S., 2015. Pseudo-turbulent gas-phase velocity fluctuations in homogeneous gas–solid flow: fixed particle assemblies and freely evolving suspensions. Journal of Fluid Mechanics 770, 210–246.

[34] Mehta, M., Sengupta, A., Renno, N.O., Norman, J.W.V., Huseman, P.G., Gulick, D.S., Pokora, M., 2013. Thruster plume surface interactions: Applications for spacecraft landings on planetary bodies. AIAA Journal 51, 2800–2818.

[35] Mehta, Y., Jackson, T.L., Balachandar, S., 2019a. Pseudo-turbulence in inviscid simulations of shock interacting with a bed of randomly distributed particles. Shock Waves , 1–14.

[36] Mehta, Y., Neal, C., Jackson, T., Balachandar, S., Thakur, S., 2016. Shock interaction with three-dimensional face centered cubic array of particles. Physical Review Fluids 1, 054202.

[37] Mehta, Y., Neal, C., Salari, K., Jackson, T.L., Balachandar, S., Thakur, S., 2018. Propagation of a strong shock over a random bed of spherical particles. Journal of Fluid Mechanics 839, 157–197.

[38] Mehta, Y., Salari, K., Jackson, T.L., Balachandar, S., 2019b. Effect of Mach number and volume fraction in air-shock interacting with a bed of randomly distributed spherical particles. Physical Review Fluids 4, 014303.

[39] Osnes, A.N., Vartdal, M., Omang, M.G., Reif, B.A.P., 2019. Computational analysis of shock-induced flow through stationary particle clouds. International Journal of Multiphase Flow 114, 268–286.

[40] Park, G.I., Bassenne, M., Urzay, J., Moin, P., 2017. A simple dynamic subgrid-scale model for LES of particle-laden turbulence. Physical Review Fluids 2, 044301.

[41] Parmar, M., Haselbacher, A., Balachandar, S., 2010. Improved drag correlation for spheres and application to shock-tube experiments. AIAA Journal 48, 1273–1276.

[42] Patankar, N., Joseph, D., 2001. Modeling and numerical simulation of particulate flows by the Eulerian-Lagrangian approach. International Journal of Multiphase Flow 27, 1659–1684.

[43] Peng, C., Kong, B., Zhou, J., Sun, B., Passalacqua, A., Subramaniam, S., Fox, R.O., 2019. Implementation of pseudo-turbulence closures in an Eulerian–Eulerian two-fluid model for non-isothermal gas–solid flow. Chemical Engineering Science 207, 663–671.

[44] Pepiot, P., Desjardins, O., 2012. Numerical analysis of the dynamics of two-and three-dimensional fluidized bed reactors using an Euler–Lagrange approach. Powder Technology 220, 104–121.

[45] Regele, J.D., Rabinovitch, J., Colonius, T., Blanquart, G., 2014. Unsteady effects in dense, high speed, particle laden flows. International Journal of Multiphase Flow 61, 1–13.

[46] Schneiderbauer, S., Saeedipour, M., 2018. Approximate deconvolution model for the simulation of turbulent gas-solid flows: An a priori analysis. Physics of Fluids 30, 023301.

[47] Schneiderbauer, S., Saeedipour, M., 2019. Numerical simulation of turbulent gas-solid flow using an approximate deconvolution model. International Journal of Multiphase Flow .

[48] Sen, O., Gaul, N.J., Davis, S., Choi, K.K., Jacobs, G., Udaykumar, H.S., 2018. Role of pseudo-turbulent stresses in shocked particle clouds and construction of surrogate models for closure. Shock Waves , 1–19.

[49] Shallcross, G.S., Capecelatro, J., 2018. A parametric study of particle-laden shock tubes using an Eulerian–Lagrangian framework, in: 2018 AIAA Aerospace Sciences Meeting, p. 2080.

[50] Stolz, S., Adams, N.A., 1999. An approximate deconvolution procedure for large-eddy simulation. Physics of Fluids 11, 1699–1701.

[51] Strand, B., 1994. Summation by parts for finite difference approximations for d/dx. Journal of Computational Physics 110, 47–67.

[52] Sun, B., Tenneti, S., Subramaniam, S., 2015. Modeling average gas–solid heat transfer using particle-resolved direct numerical simulation. International Journal of Heat and Mass Transfer 86, 898–913.

[53] Sutkar, V.S., Deen, N.G., Patil, A.V., Salikov, V., Antonyuk, S., Heinrich, S., Kuipers, J.A.M., 2016. CFD–DEM model for coupled heat and mass transfer in a spout fluidized bed with liquid injection. Chemical Engineering Journal 288, 185–197.

[54] Svärd, M., 2004. On coordinate transformations for summation-by-parts operators. Journal of Scientific Computing 20, 29–42.

[55] Svärd, M., Carpenter, M.H., Nordström, J., 2007. A stable high-order finite difference scheme for the compressible Navier–Stokes equations, far-field boundary conditions. Journal of Computational Physics 225, 1020–1038.

[56] Taverniers, S., Udaykumar, H., Jacobs, G.B., 2019. Two-way coupled Cloud-In-Cell modeling of non-isothermal particle-laden flows: A Subgrid Particle-Averaged Reynolds Stress-Equivalent (SPARSE) formulation. Journal of Computational Physics 390, 595–618.

[57] Tenneti, S., Garg, R., Subramaniam, S., 2011. Drag law for monodisperse gas–solid systems using particle-resolved direct numerical simulation of flow past fixed assemblies of spheres. International Journal of Multiphase Flow 37, 1072–1092.

[58] Tenneti, S., Subramaniam, S., 2014. Particle-resolved direct numerical simulation for gas-solid flow model development. Annual Review of Fluid Mechanics 46, 199–230.

[59] Tenneti, S., Sun, B., Garg, R., Subramaniam, S., 2013. Role of fluid heating in dense gas–solid flow as revealed by particle-resolved direct numerical simulation. International Journal of Heat and Mass Transfer 58, 471–479.

[60] Theofanous, T.G., Chang, C.H., 2017. The dynamics of dense particle clouds subjected to shock waves. Part 2. Modeling/numerical issues and the way forward. International Journal of Multiphase Flow 89, 177–206.

[61] Theofanous, T.G., Mitkin, V., Chang, C.H., 2018. Shock dispersal of dilute particle clouds. Journal of Fluid Mechanics 841, 732–745.

[62] Tukey, J.W., 1967. An introduction to the calculation of numerical spectrum analysis. Spectra Analysis of Time Series , 25–46.

[63] Uhlmann, M., 2005. An immersed boundary method with direct forcing for the simulation of particulate flows. Journal of Computational Physics 209, 448–476.

[64] Vassilicos, J.C., 2015. Dissipation in turbulent flows. Annual Review of Fluid Mechanics 47, 95–114.

[65] Vishnampet Ganapathi Subramanian, R., 2015. An exact and consistent adjoint method for high-fidelity discretization of the compressible flow equations. Ph.D. thesis. University of Illinois at Urbana-Champaign.

[66] Wagner, J.L., Beresh, S.J., Kearney, S.P., Trott, W.M., Castaneda, J.N., Pruett, B.O., Baer, M.R., 2012. A multiphase shock tube for shock wave interactions with dense particle fields. Experiments in Fluids 52, 1507–1517.

[67] Watanabe, T., Sakai, Y., Nagata, K., Ito, Y., Hayase, T., 2015. LES–Lagrangian particle method for turbulent reactive flows based on the approximate deconvolution model and mixing model. Journal of Computational Physics 294, 127–148.

[68] Xia, Z., Shi, Y., Zhang, Q., Chen, S., 2016. Modulation to compressible homogenous turbulence by heavy point particles. i. effect of particles density. Physics of Fluids 28, 016103.

[69] Zhang, D., Prosperetti, A., 1997. Momentum and energy equations for disperse two-phase flows and their closure for dilute suspensions. International Journal of Multiphase Flow 23, 425–453.